



Weathering of the Rio Blanco quartz diorite, Luquillo Mountains, Puerto Rico: Coupling oxidation, dissolution, and fracturing

Heather L. Buss^{a,*}, Peter B. Sak^b, Samuel M. Webb^c, Susan L. Brantley^d

^a U.S. Geological Survey, 345 Middlefield Road, MS 420, Menlo Park, CA 94025, USA

^b Department of Geology, Dickinson College, Carlisle, PA 17013, USA

^c Stanford Synchrotron Radiation Laboratory, Stanford Linear Accelerator Center, 2525 Sand Hill Road, MS 69, Menlo Park, CA 94025, USA

^d Earth and Environmental Systems Institute, Penn State University, University Park, PA 16802, USA

Received 13 September 2007; accepted in revised form 10 June 2008; available online 4 July 2008

Abstract

In the mountainous Rio Icacos watershed in northeastern Puerto Rico, quartz diorite bedrock weathers spheroidally, producing a 0.2–2 m thick zone of partially weathered rock layers (~2.5 cm thickness each) called rindlets, which form concentric layers around corestones. Spheroidal fracturing has been modeled to occur when a weathering reaction with a positive ΔV of reaction builds up elastic strain energy. The rates of spheroidal fracturing and saprolite formation are therefore controlled by the rate of the weathering reaction.

Chemical, petrographic, and spectroscopic evidence demonstrates that biotite oxidation is the most likely fracture-inducing reaction. This reaction occurs with an expansion in $d(001)$ from 10.0 to 10.5 Å, forming “altered biotite”. Progressive biotite oxidation across the rindlet zone was inferred from thin sections and gradients in K and Fe(II). Using the gradient in Fe(II) and constraints based on cosmogenic age dates, we calculated a biotite oxidation reaction rate of 8.2×10^{-14} mol biotite $\text{m}^{-2} \text{s}^{-1}$. Biotite oxidation was documented within the bedrock corestone by synchrotron X-ray microprobe fluorescence imaging and XANES. X-ray microprobe images of Fe(II) and Fe(III) at 2 μm resolution revealed that oxidized zones within individual biotite crystals are the first evidence of alteration of the otherwise unaltered corestone.

Fluids entering along fractures lead to the dissolution of plagioclase within the rindlet zone. Within 7 cm surrounding the rindlet–saprolite interface, hornblende dissolves to completion at a rate of 6.3×10^{-13} mol hornblende $\text{m}^{-2} \text{s}^{-1}$: the fastest reported rate of hornblende weathering in the field. This rate is consistent with laboratory-derived hornblende dissolution rates. By revealing the coupling of these mineral weathering reactions to fracturing and porosity formation we are able to describe the process by which the quartz diorite bedrock disaggregates and forms saprolite. In the corestone, biotite oxidation induces spheroidal fracturing, facilitating the influx of fluids that react with other minerals, dissolving plagioclase and chlorite, creating additional porosity, and eventually dissolving hornblende and precipitating secondary minerals. The thickness of the resultant saprolite is maintained at steady state by a positive feedback between the denudation rate and the weathering advance rate driven by the concentration of pore water O_2 at the bedrock–saprolite interface.

© 2008 Elsevier Ltd. All rights reserved.

1. INTRODUCTION

Rock weathering is the initial step in the soil-forming process and the primary contributor of chemical solutes to the hydrosphere. The boundaries at which weathering transforms intact bedrock into disaggregated regolith

* Corresponding author.

E-mail addresses: hlbuss@usgs.gov (H.L. Buss), sakp@dickinson.edu (P.B. Sak), samwebb@slac.stanford.edu (S.M. Webb), brantley@eesi.psu.edu (S.L. Brantley).

(such as saprolite) are complex interfaces controlled by coupled chemical, physical, and microbial processes driven by the flux of reactants into the bedrock. The rate of rock weathering determines the advance rate of the bedrock–saprolite interface and, in a steady state profile, the rate of formation of soil. In turn, the rates of individual geochemical reactions contribute to the bedrock weathering rate, the flux of mineral nutrients to the biosphere, and the flux of solutes to the hydrosphere.

Soils developed on granite, sandstone, and metamorphosed crystalline bedrock have often been presumed to be in steady state with respect to thickness (e.g., Brown et al., 1995; Heimsath et al., 1999; von Blanckenburg et al., 2004), regolith formation, erosion, weathering (e.g., Pavich, 1989; Brown et al., 1995; Riebe et al., 2003; Turner et al., 2003; Dosseto et al., in press), elemental concentrations (e.g., Riebe et al., 2003), and yearly averaged biomass and organic carbon (Buss et al., 2005). If indeed the total mass of regolith (including saprolite) in a profile is constant in time, then conservation of mass requires that the rate of formation of regolith equals the total denudation rate, and thus the sum of the rates of chemical weathering and physical erosion. In an isovolumetric weathering profile (such as a saprolite), steady state mass is equivalent to steady state thickness. In the granitic Rio Icacos watershed in Puerto Rico, Brown et al. (1995) estimated a long-term average total denudation rate of $43 \text{ m Ma}^{-1} \pm 35\%$ based on cosmogenic ^{10}Be accumulations in the stream sediments, consistent with later estimates by White et al. (1998) and Riebe et al. (2003) using combinations of cosmogenic nuclide and geochemical mass balance methods. White et al. (1998) calculated the rate of regolith formation (also known as the *weathering advance rate*) as 58 m Ma^{-1} based on the watershed solute flux normalized to the geographical surface area (expressed as unit regolith surface area). The agreement of these rates supports the assumption of a steady state regolith profile. Thus, the total denudation rate is commonly equated with the rate of bedrock transformation to regolith for the Rio Icacos watershed and other sites where weathering is assumed to be occurring at steady state (e.g., Murphy et al., 1998; White et al., 1998; Riebe et al., 2003; Turner et al., 2003; Buss et al., 2005; Fletcher et al., 2006).

Although steady state assumptions are frequently used in models the coupling between erosion and weathering advance rates is difficult to understand. Fletcher et al. (2006) proposed that the rate at which saprolite is created from the Rio Icacos bedrock is controlled by the chemistry of pore fluids at depth and that this chemistry is in turn controlled by the thickness of the regolith profile. Pore fluid O_2 may diffuse into the bedrock, oxidizing Fe(II)-bearing primary minerals, creating elastic strain that spheroidally fractures the Rio Icacos bedrock (Fletcher et al., 2006). In many locations such as Rio Icacos, bedrock disaggregates to regolith at spheroidally weathering interfaces. Geochemical reactions involving Fe-silicate minerals have been credited with causing the fracturing that initiates regolith formation at such interfaces (e.g., Larsen, 1948; Simpson, 1964; Egler et al., 1969; Isherwood and Street, 1976;

Chatterjee and Raymahashay, 1998; Scarciglia et al., 2005; Fletcher et al., 2006).

Fletcher et al. (2006) proposed that oxidation of hornblende (where $\Delta V_{\text{reaction}} > 0$) drives fracturing and controls the rate of weathering advance. Given that dissolved O_2 in soil pore waters decreases with depth, they pointed out that deeper soils would have slower weathering advance rates than shallower soils. Their model is consistent with pore water dissolved O_2 as the parameter that couples erosion to the weathering advance rate. Herein we present a detailed geochemical investigation of the spheroidally weathering bedrock–saprolite interface in the Rio Icacos watershed. Specifically we examine the occurrence and rates of individual mineral weathering reactions within the spheroidally fractured zone, with particular emphasis on the Fe-silicate minerals, in order to identify the fracture-initiating reaction, to understand the relationships between specific reactions and porosity development, and to quantify the flux of Fe(II) from weathering bedrock.

1.1. Spheroidal weathering

Spheroidal weathering refers to a well known but poorly understood type of exfoliation in which corestones are surrounded by concentric layers of weathering rock (Ollier, 1971). Corestones are blocks of residual bedrock that are weathered in place along pre-existing joint planes, rounding off corners to create boulders (Linton, 1955; Ollier, 1971). The concentric layers surrounding corestones are variously called sheets, layers, shells, plates, scales, or rindlets (Bisdom, 1967; Ollier, 1971; Fritz and Ragland, 1980). Envisioning an entire sequence of layers as a weathering rind, here we adopt the term rindlets to describe the individual layers consistent with terminology used by Fritz and Ragland (1980), Turner et al. (2003), Buss et al. (2005), and Fletcher et al. (2006). We also refer to a complete set of rindlets as a rindlet zone (Figs. 1 and 2).

Spheroidal weathering is most common in homogeneous, jointed, competent rocks, primarily granite and basalt although it has also been observed on gneisses, schists, andesites, sandstones, and greywackes (e.g., Ollier, 1967; Heald et al., 1979; Fritz and Mohr, 1984; Chatterjee and Raymahashay, 1998). Granitic corestones are found in a variety of climatic regions on all continents except Antarctica and thus represent a widespread phenomenon impacting regolith formation worldwide.

Large-scale exfoliation structures such as tors or domes in the Sierra Nevada have long been thought to be created by the dilation induced by the relief of stress during erosional unloading (e.g., Gilbert, 1904; Farmin, 1937; Schattner, 1961; Thomas, 1974), a mechanism thought to be independent of—although aggravated by—surficial processes such as hydration and freeze–thaw (e.g., Farmin, 1937). Spheroidal weathering has often been recognized as a different, or special, case of exfoliation and has been attributed to surficial processes, most commonly chemical weathering (Farmin, 1937; Ollier, 1971; Fletcher et al., 2006). It is unclear why some rocks weather spheroidally and others do not. Some investigators have proposed that the percentage of biotite (Le Pera and Sorriso-Valvo,

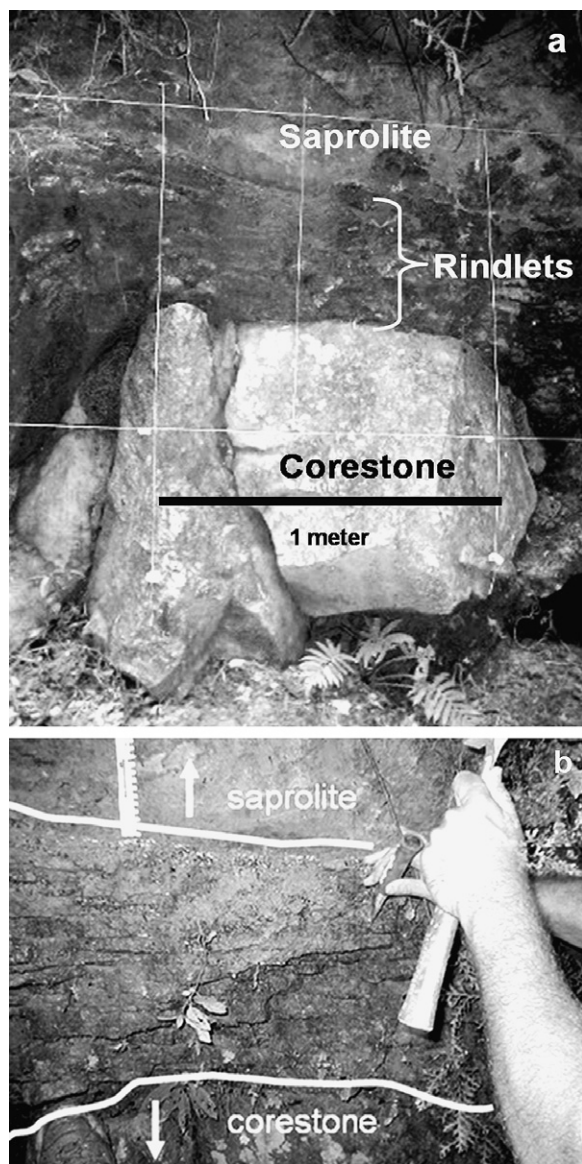


Fig. 1. (a) Photograph of the primary sampling site along a roadcut on Route 191 (see map, Fig. 3). Here the ~1 m diameter corestone is surrounded by ~50 cm zone of rindlets and ~2 m of saprolite. (b) From Buss et al. (2004), close up photograph of the top of the corestone pictured in (a). The sub-horizontal rindlet sequence pictured was sampled in the present study.

2000) or feldspar (Ferry, 1984) controls susceptibility to spheroidal weathering and others have argued for (Isherwood and Street, 1976; Sequeira Braga et al., 2002) or against (Ollier, 1988; Romani and Twidale, 1998; Mignon and Thomas, 2002) climatic controls. A number of researchers have suggested that dilation during mineral weathering could induce spheroidal fracturing or fracture-induced disintegration (e.g., Larsen, 1948; Simpson, 1964; Egger et al., 1969; Isherwood and Street, 1976; Begle, 1978; Bustin and Mathews, 1979; Chatterjee and Raymahashay, 1998; Fletcher et al., 2006). Ollier (1967) argues that a net volume change is unlikely because the rocks retain joint and mineral structure after spheroidal cracking. Indeed,

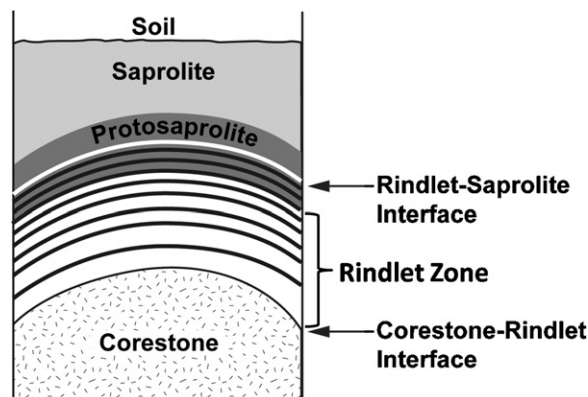


Fig. 2. Simplified diagram of the weathering profile in the Rio Icacos watershed. The quartz diorite bedrock is rounded into corestones, which fracture concentrically forming a ~0.2–2 m thick rindlet zone, overlain by 2–8 m of saprolite and 0.5–1 m of soil. The area immediately surrounding the rindlet–saprolite interface is here called the “protosaprolite zone”.

spheroidal weathering often produces saprolite, which is defined as an isovolumetric weathering product. Fletcher et al. (2006) demonstrated quantitatively that only a very small net volume change is required to generate a build-up of elastic strain energy sufficient to produce the fractures that define individual rindlets.

Fletcher et al. (2006) postulated that a positive $\Delta V_{\text{reaction}}$ ($\Delta V_{\text{reaction}} = \sum V_{\text{products}} - \sum V_{\text{reactants}}$) for the precipitation of ferric oxides after the oxidation of ferrous minerals builds up elastic strain energy in the rock, which causes the fracturing that demarcates rindlets. In this scenario, the rate of spheroidal weathering, and hence the rate of advance of the bedrock–saprolite interface (the rindlet zone), is a function of the concentrations of ferrous minerals and oxygen, the reaction rate, the rate of transport, and the mechanical properties of the rock. Fletcher et al. (2006) proposed that the dissolution of hornblende in a granitic rock coupled with a precipitation of ferrihydrite could yield a positive $\Delta V_{\text{reaction}}$. However, there are several possible reactions involving ferrous minerals common to granitic rocks that could produce a ferric product: dissolution of hornblende, biotite, or augite followed by precipitation of a ferric (hydr)oxide mineral, or solid-phase oxidation of Fe(II) within hornblende, biotite, or augite. In the present paper we seek to identify the first weathering reaction that occurs in the corestones in order to refine the model presented in Fletcher et al. (2006) and to identify controls on the thickness of the rindlet zone and its transformation to saprolite.

In a spheroidally weathering system, a rindlet sequence defines the bedrock–saprolite interface, where bedrock chemically weathers and disaggregates to form saprolite (Fig. 2). For an assumed steady state system such as the Rio Icacos weathering profile (Brown et al., 1995; Riebe et al., 2003; Fletcher et al., 2006), the rate of formation of the saprolite is equal to the movement of the boundary between the saprolite and the bedrock and to the total denudation rate. This boundary moves downward into the bedrock as rindlets form during spheroidal weathering.

Turner et al. (2003) conceptualized the Rio Icacos weathering profile as multiple parallel weathering fronts that advance inward towards the center of the corestones as well as inward from inter-rindlet boundaries towards the rindlet centers. In this model, the net rate of advance of the multiple rindlet-scale fronts equals the net rate of advance of the corestone-scale front. Likewise, the net rate of advance of the corestone-scale front equals the total denudation rate. If the rindlet-bounding fractures are a series of parallel weathering fronts (as per Turner et al., 2003), then chemical and mineralogical trends should be measurable across a single rindlet. That is, weathering intensity should decrease markedly from a rindlet's edges towards the rindlet's interior. In this case, the weathering advance rate would be the sum of the rates of the individual parallel rindlet fronts. Alternatively, the entire rindlet zone could be a single weathering front with only two controlling interfaces: the bedrock-rindlet interface and the rindlet-saprolite interface (Fig. 2).

1.2. Field site and sample collection

The Rio Icacos watershed in Puerto Rico's Luquillo Experimental Forest is located on Rio Blanco quartz diorite bedrock mantled by 200 ka regolith, which was dated using ^{10}Be (Brown et al., 1995). The regolith is composed of 2–8 m of saprolite and 0.5–1 m of soil. These Picachociales complex soils, previously classified as ultisols (Boccheciamper et al., 1977), are now considered inceptisols due to weak B horizon development, despite being highly weathered (USDA NCRS, 2002). The quartz diorite weathers spheroidally forming corestones that average 2 m in diameter, surrounded by 0.2–2 m rindlet zones containing individual rindlets of 2.6 cm average thickness (Turner et al., 2003; Buss et al., 2004, 2005; Fletcher et al., 2006).

The Rio Blanco quartz diorite bedrock contains zoned plagioclase, quartz, hornblende, partially chloritized biotite, and minor primary iron oxides and accessory minerals (Murphy et al., 1998; White et al., 1998). The overlying saprolite contains kaolinite, goethite, quartz, and biotite. Biotite weathering occurs in two stages via two mechanisms. First, an "altered biotite" phase forms that has a larger d (001) spacing, and higher Al/Si and Fe(III)/Fe(II) ratios, and less Fe, Mg, and K than fresh biotite (Dong et al., 1998; Murphy et al., 1998). This phase was detected in the saprolite, but not in the fresh rock (Dong et al., 1998). Next, altered biotite weathers to kaolinite in the saprolite either via epitaxial overgrowth of two layers of kaolinite onto one layer of altered biotite or in a 1:1 ratio with the formation of an intermediate halloysite layer (Dong et al., 1998; Murphy et al., 1998). Within the rindlet zone, plagioclase, hornblende, and chlorite must weather completely because these minerals are not found in the saprolite (Murphy et al., 1998; White et al., 1998; Turner et al., 2003). In the present paper we explore the weathering reactions occurring within the rindlet zone and at all of the interfaces associated with the rindlet zone: corestone-rindlet, rindlet-saprolite, and the multiple parallel rindlet-rindlet interfaces.

In June 2003 and July 2004 we collected a suite of solid samples from the Rio Icacos watershed including saprolite, corestone, and rindlets (Figs. 1 and 2). Rindlets were sampled from around a corestone exposed at a roadcut on Route 191 (Fig. 3). The samples include the edge of a corestone and a continuous 49 cm section of rindlets above the corestone, spanning the entire rindlet sequence between corestone and saprolite. The corestone samples were collected using a sledgehammer. The rindlet samples were carefully removed with a hammer and chisel, wrapped in plastic and packing tape, and labeled according to position and orientation. At the rindlet-saprolite interface, the rindlets are more friable, thinner, and lighter in color than the majority of the rindlet zone. Likewise, the saprolite just above the interface is slightly harder and darker in color than the bulk of the overlying saprolite. This 7 cm thick zone, consisting of four ~ 1 cm thick, highly weathered rindlets and roughly 3 cm of adjacent saprolite, we term the protosaprolite zone (Fig. 2). The rindlet-saprolite interface runs through the protosaprolite zone. In this outcrop, we refer to the rindlet zone as the ~ 46 cm region containing all of the hard, cohesive rindlets between the corestone and the protosaprolite zone. Rindlet-bounding fractures anastomose and outer rindlets (further from the corestone) tend to split, complicating precise definition of a single rindlet. Therefore, samples bounded by parallel fractures along a chosen transect were defined as individual rindlets. Where the transect crossed anastomosing fractures or partially split rindlets, the sample was collected as a single piece and considered a single rindlet. Delicate saprolite and protosaprolite samples were coated with melted wax on at least one side before removal from the outcrop to preserve the structure and orientation.

2. ANALYTICAL METHODS

2.1. Sample preparation and analysis

Bulk densities of the rindlet samples were determined by coating samples with thin layers of rubber cement and immersing them in water to measure volume displacement. Bulk elemental analysis was performed on pulverized and sieved ($150\ \mu\text{m}$) corestone, rindlet, and saprolite samples. These analyses included major and minor elements by inductively coupled plasma atomic emission spectrometry (ICP-AES) after lithium metaborate fusion digestion and FeO by titration after a multi-acid digest (SGS Mineral Laboratories, Ontario, Canada). Subsamples from within individual rindlets were taken by careful grinding with a Dremel rotary tool equipped with diamond points.

Minerals within thin sections prepared from each rindlet were identified using optical microscopy and electron probe microanalysis (EPMA, Cameca SX-50). EPMA was also used to measure the composition of crystals as a function of distance from the corestone and from rindlet edges. Backscattered electron (BSE) images, mosaic maps of BSE images, and X-ray elemental maps of the thin sections were made on an FEI Quanta 400 SEM equipped with an energy dispersive X-ray spectrometer (EDS). Modal analysis was performed on backscattered images using XT-Docu

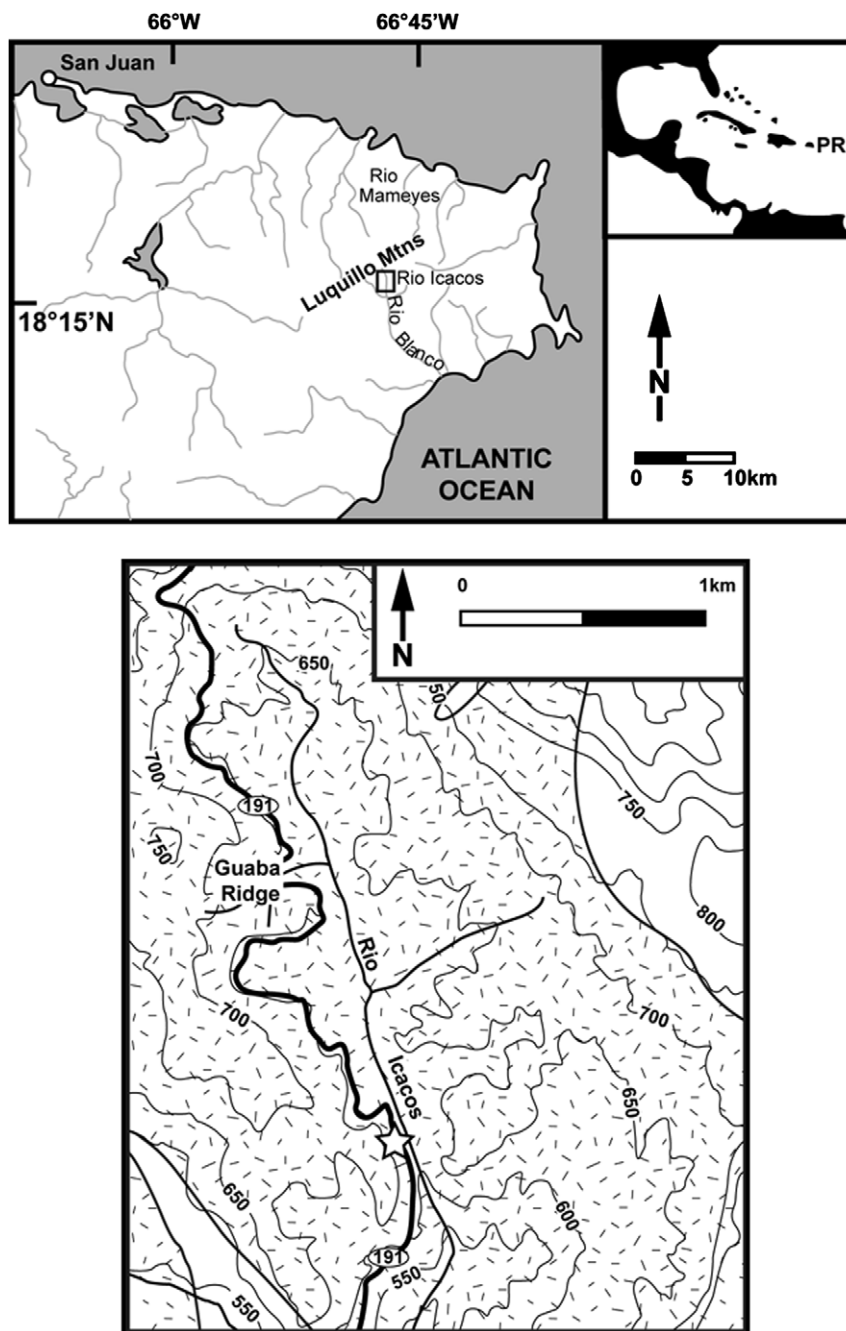


Fig. 3. Maps of the field area. A star indicates location of the sampled road cut.

software (v. 3.2, Soft-Imaging System GmbH, Münster, Germany) to point count phases identified by the user based on the backscatter grayscale value and crystal morphology. This technique has been used to measure porosity in weathering rinds (Dorn, 1995; Dixon et al., 2006). To supplement microscopic phase identification in the highly weathered rindlets and in the protosaprolite zone, X-ray diffraction (XRD) was performed on randomly oriented, powdered samples on a Scintag X2 theta–theta goniometer with a copper target. A step scan was used with a step size of 0.02° and 2 s per step.

2.2. X-ray microprobe imaging

To look for incipient oxidation reactions within Fe(II)-containing phases in the corestone that may be too small to identify with the above mentioned techniques, synchrotron micro-fluorescence maps of mineral grains in thin sections were made at the Stanford Synchrotron Radiation Laboratory (SSRL) on Beam Line 2.3. This technique permits identification of microscale spatial variations in oxidation state and stoichiometry within single mineral grains. Beam size on the sample was approximately $2 \times 2 \mu\text{m}$ at

full width half maximum using Kirkpatrick-Baez (K-B) focusing optics (X-Radia). X-ray fluorescence data were recorded using a single element Si Vortex detector (SSI). Monochromatic X-rays were selected using a water cooled Si(220) $\phi = 0$ double crystal monochromator. The X-ray energy was calibrated to the first inflection point of an Fe metal foil, $E = 7112$ eV. Maps were collected at several incident energies (7121, 7125, 7130, and 7142 eV) in continuous raster scanning mode in order to collect the fluorescence at several distinguishing points within the Fe edge to determine Fe oxidation states in the sample. Fluorescence maps were analyzed using the Microanalysis Toolkit (Webb, 2006). Fe and K fluorescence counts were normalized to the measured intensity of the incident X-ray beam (I_0). The proportion of Fe(II) and Fe(III) at each point in the map was determined by linear least squares analysis based on the normalized fluorescence spectra of Fe(II) (0.2 M $\text{Fe}(\text{NH}_4)_2(\text{SO}_4)_2$ solution) and Fe(III) (Fe_2O_3) standards. X-ray absorption near edge spectra (XANES) were collected on the same beam line on spots of interest and microprobe data were fitted to XANES spectra (Webb, 2006) to confirm phase identification.

2.3. Mass transfer calculations

In a weathering profile, the mass of an immobile element is, by definition, the same in both the parent rock and the weathered material for some volume of material. However, the mass fraction of the immobile element (e.g., g Ti g^{-1} saprolite) in the weathered material will differ from that in the parent if weathering processes have resulted in a change in density. By comparing the mass fractions of mobile elements that of an immobile element the mass transfer (loss or gain of an element relative to the parent rock composition) can be documented (e.g., Brimhall and Dietrich, 1987; Anderson et al., 2002).

Mass transfer of individual elements relative to Ti was calculated for each rindlet and saprolite sample. Open-system mass transport is quantifiable in the present samples because the parent material is homogenous (Rio Blanco quartz diorite), of uniform age (Tertiary), and contains a relatively inert component (Ti) that is present in both the parent and product material (Chadwick et al., 1990). Because saprolite is isovolumetrically weathered rock, volumetric strain (change in volume as a result of stress), calculated on the basis of an assumed immobile element, should be near-zero. White et al. (1998) identified Ti as relatively immobile in the Puerto Rican saprolite relative to the bedrock. The relative immobility of Ti in the rindlet zone was confirmed by our calculations of very low volumetric strain with respect to Ti:

$$\varepsilon_{\text{Ti,w}} = \frac{\rho_p C_{\text{Ti,p}}}{\rho_w C_{\text{Ti,w}}} - 1 \quad (1)$$

where $\varepsilon_{\text{Ti,w}}$ is the volumetric strain in the weathered (w) sample with respect to Ti, ρ_w is the bulk density of the weathered material (rindlets), ρ_p is bulk density of the parent (p) rock, $C_{\text{Ti,w}}$ is the mass fraction of Ti in the weathered material, and $C_{\text{Ti,p}}$ is the mass fraction of Ti in the parent rock. Ti occurs in the Rio Blanco quartz diorite par-

ent rock as ilmenite and as a structural component of biotite that is not lost from the biotite lattice during weathering (Murphy et al., 1998). Thus, we assume Ti to be immobile in order to estimate mass loss during weathering.

Mass transfer (gain or loss) of an element j relative to the parent rock, represented by the mass transfer coefficient, $\tau_{\text{Ti},j}$, can be calculated as:

$$\tau_{\text{Ti},j} = \left(\frac{C_{j,w} C_{\text{Ti,p}}}{C_{j,p} C_{\text{Ti,w}}} \right) - 1 \quad (2)$$

Here, $C_{j,w}$ is the mass fraction of element j in the weathered material, and $C_{j,p}$ is the mass fraction of element j in the parent material. If $\tau_{\text{Ti},j} = -1$, element j is entirely lost. If $\tau_{\text{Ti},j} > 0$, a net gain of element j relative to the parent rock is indicated. The average of five analyses from a single core-stone was used in the present calculations as the parent rock composition.

3. RESULTS

3.1. Porosity development

Three types of cracks were observed in the system and will be referred to as macro-cracks, rindlet micro-cracks, and grain micro-cracks. The macro-cracks demarcate individual rindlets, run subparallel to the corestone-rindlet interface, and are easily observed in the outcrop (Fig. 1). Rindlet micro-cracks, found within every rindlet we examined, are contained within individual rindlets, are not preferentially aligned, are not associated with any given mineral, and cut across multiple crystals of all phases indiscriminately. Density, length, and width of rindlet micro-cracks increase with distance away from the corestone, towards the saprolite (Fig. 4). In the rindlets closest to the corestone, apertures of rindlet micro-cracks are $< 10 \mu\text{m}$ wide and short (rarely extending across an entire 6 mm^2 SEM image). From about 20 cm above of the corestone (about halfway between the corestone and the saprolite) and beyond, rindlet micro-cracks that are 25–90 μm wide are common, with some as large as 250 μm wide (Fig. 4c). By this point it becomes difficult to image a 6 mm^2 area that does not contain rindlet micro-cracks that span the image. Rindlet micro-cracks were not observed within the corestone.

Grain micro-cracks are associated with individual mineral grains and are typically observed along cleavage planes or along grain boundaries. Grain micro-cracks are found throughout all rindlets and are most noticeable within $\sim 5 \text{ mm}$ of the macro-cracks (along the edges of every rindlet). Within the outer 9 or 10 mm of the corestone, occasional grain micro-cracks are identifiable. No micro-cracks are recognized more than 10 mm into the corestone.

The bulk density decreases steadily across the rindlet zone, from 2.7 g cm^{-3} for the corestone to 1.8 g cm^{-3} at the rindlet-saprolite interface (Fig. 5a), and mirrors the increase in porosity determined by point counting (Fig. 5b). Porosity and low molecular weight pore-filling precipitates were readily distinguished from the crystalline phases using EDS and SEM. To limit variability in the point counts due

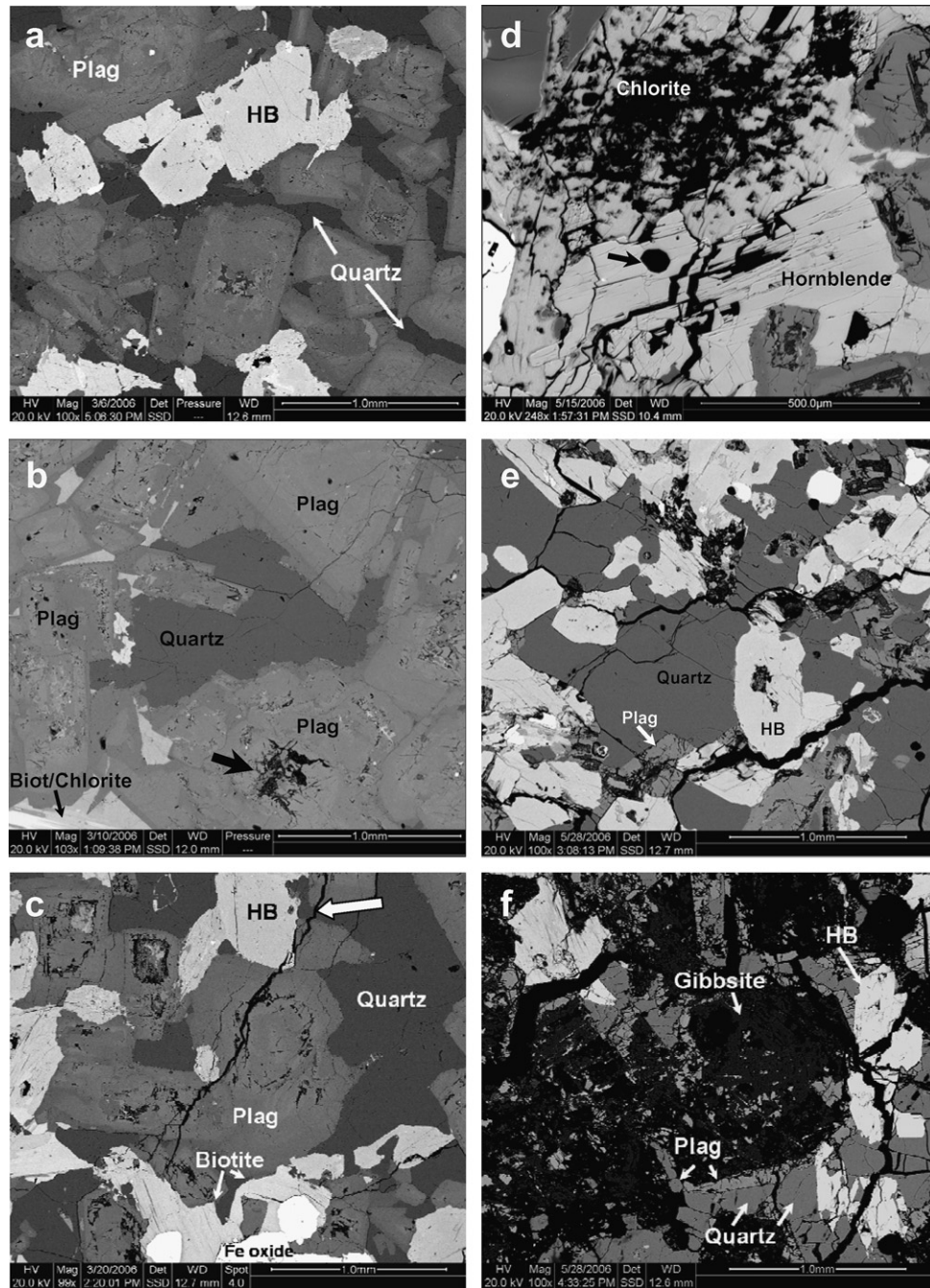


Fig. 4. Backscattered electron (BSE) images of thin sections. (a) Large zoned plagioclase crystals dominate the un-fractured, apparently un-weathered corestone. (b) In a rindlet ~8 cm above the corestone–rindlet interface, occasional zoned plagioclase crystals partially dissolve and form secondary precipitates within the interior of the crystals (shown with the thick black arrow), quartz crystals are pristine, and partially chloritized biotite grains show no signs of dissolution or alteration in BSE images. (c) A rindlet sampled from ~20 cm above the corestone is typical of most rindlets: all rindlets have rindlet micro-cracks (an example is shown with a white arrow) that cut across multiple crystals while most hornblende crystals remain visibly un-altered throughout the majority of the rindlet zone. (d) In the last intact rindlet below the protosaprolite zone, ~47 cm above the corestone–rindlet interface, chlorite is highly weathered, and hornblende, although cracked, shows no obvious dissolution features. The arrow points to a round hole within the hornblende where an apatite inclusion is believed to have dissolved without affecting the adjoining hornblende (sub-spheroidal apatite inclusions are commonly observed in the unaltered corestone). Note the difference in scale of this image. (e) In the protosaprolite zone, ~2 cm below the rindlet–saprolite interface, plagioclase crystals are highly weathered and hornblende crystals show the first signs of dissolution. Quartz remains visibly un-altered throughout the rindlet and protosaprolite zones. (f) In the protosaprolite zone, ~1 cm below the rindlet–saprolite interface, the plagioclase is almost entirely lost, much of the pore space created by dissolution of primary minerals is filled with gibbsite, and to a lesser extent, kaolinite. Here hornblende crystals are significantly smaller than they are in the corestone.

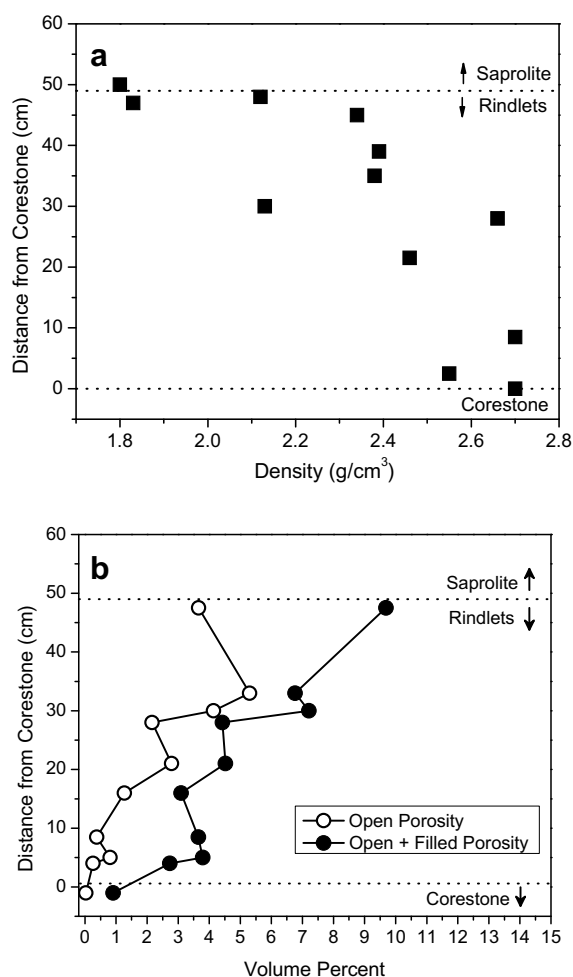


Fig. 5. (a) Individual rindlets show a steady decrease in bulk density as a function of distance from the corestone. (b) Volume percent open porosity and total porosity (including low molecular weight secondary precipitates such as gibbsite filling pore spaces) determined by point counting using XT Docu software on backscattered electron images.

to large rindlet micro-cracks and image resolution, porosity and mineral phases in the majority of the rindlet zone were only counted on same-size BSE images ($\sim 6 \text{ mm}^2$ areas) that did not contain rindlet micro-cracks that spanned the entire image. However, the extensive network of micro-cracks made this impossible in the outermost. For these samples, care was taken to avoid micro-cracks larger than $\sim 60 \mu\text{m}$ wide.

Porosity in the corestone is extremely low (0.03%) at approximately 36 mm below the corestone–rindlet interface. Throughout the rindlet zone, non-crack porosity is dominated by intra-crystal weathering of the hydrothermally altered calcic cores of zoned plagioclase crystals (Fig. 4b). Additional porosity is created by apatite crystals, which weather inward from the edges, forming apatite-shaped pores (Fig. 4d). Apatite crystals are mostly present as inclusions within hornblende and biotite and less commonly within primary iron oxides. They are also found adjacent to other primary minerals. With increasing

distance from the corestone, apatite content decreases, while the abundance of apatite-shaped pores increase.

3.2. Chemical mobility

Calculations of the mass transfer coefficient, $\tau_{Ti,j}$ (Eq. (2)), indicate the average order of cation mobility in the entire rindlet zone relative to the corestone: $\text{P} > \text{Ca} \sim \text{Na} > \text{Fe(II)} > \text{K} > \text{Mn} > \text{Si} \sim \text{Mg} > \text{Fe}$ (total) $> \text{Al}$, which differs from what has been calculated for the saprolite: $\text{Na} \approx \text{Ca} > \text{Mg} > \text{Si} > \text{K} > \text{Al} > \text{Fe}$ (total) (White et al., 1998). The most notable difference is the lower mobility of Mg in the rindlet zone relative to the saprolite. These results suggest rapid weathering of plagioclase and apatite and slower weathering of Fe-silicates (all of which contain Mg) in the rindlet zone, relative to the saprolite where Mg is lost during the weathering of biotite (Murphy et al., 1998; White et al., 1998).

Mass transfer coefficients also reveal most of the rindlets to be only slightly depleted (or enriched) in most elements relative to the corestone. The largest bulk chemical differences relative to the corestone are found in the 7 cm thick protosaprolite zone (Table 1) indicating that the majority of the chemical weathering occurs over a very narrow zone. These chemical differences correlate with the relative degree of weathering observable in BSE images (Fig. 4). These images reveal little difference between the rindlet samples and the corestone, with the exceptions of micro-cracks and plagioclase weathering in the rindlet samples. Within the protosaprolite zone, however, intense weathering is evident.

3.3. Mineralogy

The average mineralogical composition of the corestone determined by digital point counting is given in Table 2 and is consistent with previous work on the Rio Blanco quartz diorite bedrock (Seiders, 1971; Murphy et al., 1998; White et al., 1998; Turner et al., 2003). Large ($\sim 200\text{--}1000 \mu\text{m}$) plagioclase crystals with altered calcic cores are the most abundant mineral, comprising $\sim 50 \text{ vol } \%$, followed by quartz at $\sim 20 \text{ vol } \%$. The altered plagioclase cores are sericitized, typical of hydrothermal alteration. Fe-silicate phases include hornblende; biotite, which is partially replaced by chlorite; and some other chlorite that does not have a biotite morphology. The chlorite is typical of low-grade metamorphic or hydrothermal alteration. Hornblende is the most abundant Fe-silicate phase, followed by biotite. No pyroxene was observed and chlorite was relatively minor. Accessory minerals include primary Fe oxides with ilmenite exsolution lamellae, sphene, apatite, and zircon. Mineral formulas for plagioclase and the major Fe-silicate phases were determined by EPMA (Table 3).

With the exception of a slight increase in grain micro-cracking along rindlet edges, no trends in mineralogy, chemistry, or porosity were recognized across individual rindlets (e.g., Fig. 7), contradictory to the Turner et al. (2003) model of a series of multiple parallel weathering fronts made up of individual rindlets. Also, with the notable exception of apatite and, to a lesser extent, plagioclase, no distinct trend was noted in the distribution of mineral

Table 1
Mass transfer (τ_{Ti}) of elements across the rindlet and protosaprolite zones

Distance ^a	Al	Ca	Fe ^b	K	Mg	Mn	Na	P	Si	Fe(II)
<i>Rindlet zone</i>										
0.00	0.03	0.02	−0.02	0.09	−0.02	−0.04	0.03	−0.05	0.01	−0.01
0.70	−0.01	0.05	−0.05	−0.38	0.05	0.02	−0.05	−0.17	0.08	−0.13
5.50	0.79	0.58	0.02	0.68	0.17	0.04	0.88	0.05	0.59	−0.09
9.00	0.04	−0.01	0.02	−0.02	0.06	0.07	−0.02	−0.01	0.06	−0.03
14.50	−0.07	−0.23	−0.03	−0.19	−0.11	−0.05	−0.14	−0.15	−0.05	−0.23
21.50	−0.03	−0.23	0.02	−0.13	−0.05	0.02	−0.15	−0.21	−0.03	−0.21
30.00	−0.36	−0.55	−0.05	−0.20	−0.10	−0.12	−0.53	−0.64	−0.29	−0.30
39.00	−0.36	−0.58	−0.11	−0.25	−0.12	−0.16	−0.57	−0.44	−0.38	−0.33
45.00	−0.30	−0.57	−0.16	−0.16	−0.10	−0.18	−0.55	−0.37	−0.37	−0.36
47.35	−0.08	−0.08	0.02	−0.24	0.24	0.18	−0.15	−0.35	−0.01	−0.02
47.95	0.10	−0.15	−0.06	−0.13	0.02	0.01	−0.05	−0.39	0.04	−0.19
48.00	−0.11	−0.39	−0.03	−0.17	0.04	0.02	−0.38	−0.37	−0.20	−0.24
<i>Protosaprolite</i>										
48.45	0.44	−0.19	−0.02	−0.21	0.07	0.00	−0.05	−0.41	0.11	−0.14
48.75	−0.09	−0.74	−0.12	−0.29	−0.09	−0.20	−0.75	−0.82	−0.44	−0.39
49.40	−0.48	−0.81	−0.07	−0.48	−0.20	−0.29	−0.87	−0.90	−0.47	−0.41
50.20	−0.40	−0.88	−0.16	−0.60	−0.38	−0.45	−0.94	−0.95	−0.50	−0.57
51.00	−0.23	−0.90	−0.16	−0.70	−0.49	−0.52	−0.94	−0.95	−0.42	−0.65
52.00	2.13	−0.98	0.33	−0.85	−0.75	−0.36	−0.96	−1.00	0.35	−0.89

^a Distance in cm from the corestone–rindlet interface.

^b Fe is total iron.

Table 2
Average mineralogical composition^a of the corestone

Phase	Volume %
Porosity	0.03
Filled porosity ^b	0.88
Quartz	19.9
Plagioclase	49.3
Fe-silicates	24.0
Fe, Ti oxides	2.5
Apatite	0.62

^a Volume % composition determined by point counting back-scattered electron images of thin sections using image analysis software.

^b Filled porosity is very fine-grained low molecular weight material found associated with cracks or pore space. In the corestone this material is dominantly pre-existing hydrothermal alteration products rather than weathering products.

phases throughout the intact rindlet zone. Throughout the most pristine half (~25 cm) of the rindlet zone, precipitated weathering products are rare and mostly confined to plagioclase cores and along some micro-cracks. Hornblende appears pristine throughout most of the rindlet zone. Specifically, no reddening due to oxidation, no dissolution features, and no alteration to secondary phases was observed. In fact, within the majority of the rindlet zone, plagioclase and apatite inclusions commonly weather out leaving the surrounding hornblende essentially unchanged and rindlet micro-cracks commonly cross-cut hornblende crystals without evidence of chemical alteration or dissolution along the edges (Fig. 4d).

In contrast, hornblende alteration is occasionally visible about 6 cm below the rindlet–saprolite interface (in the last two intact rindlets below the protosaprolite zone). Here hornblende begins to look more reddish and some zones

Table 3
Mineral formulas measured by electron microprobe

Mineral	Formula	Sample
Hornblende	(Ca _{1.73} Na _{0.29} K _{0.06})(Mg _{2.64} Fe _{1.95} ²⁺ Mn _{0.09} Ti _{0.12} Al _{0.37})(Si _{7.24} Al _{0.76})O ₂₂ (OH) ₂	Corestone
Hornblende	(Ca _{1.57} Na _{0.26} K _{0.06})(Mg _{2.66} Fe _{1.91} ²⁺ Mn _{0.10} Ti _{0.10} Al _{0.47})(Si _{7.39} Al _{0.61})O ₂₂ (OH) ₂	Middle rindlet ^a
Hornblende	(Ca _{1.76} Na _{0.29} K _{0.07})(Mg _{2.66} Fe _{1.99} ²⁺ Mn _{0.09} Ti _{0.11} Al _{0.33})(Si _{7.21} Al _{0.79})O ₂₂ (OH) ₂	Protosaprolite
Biotite	K _{0.89} (Fe _{1.23} Fe _{0.05} ³⁺ Mg _{1.19} Mn _{0.02} Ti _{0.18} Al _{0.16})(Si _{2.88} Al _{1.12})O ₁₀ (OH) ₂	Corestone ^b
Biotite	K _{0.73} (Fe _{1.01} Fe _{0.15} ³⁺ Mg _{1.16} Mn _{0.02} Ti _{0.18} Al _{0.28})(Si _{2.88} Al _{1.12})O ₁₀ (OH) ₂	Middle rindlet
Biotite	K _{0.33} (Fe _{0.87} Fe _{0.37} ³⁺ Mg _{1.06} Mn _{0.014} Ti _{0.18} Al _{0.35})(Si _{2.87} Al _{1.13})O ₁₀ (OH) ₂	Protosaprolite
Chlorite ^c	(Mg _{3.32} Fe _{0.29} Fe _{1.00} ³⁺ Al _{1.39})(Si _{1.61} Al _{2.39})O ₁₀ (OH) ₈	Corestone
Plagioclase	Na _{0.50} Ca _{0.48} K _{0.01} Al _{1.43} Si _{2.56} O ₈	Corestone

^a The middle rindlet is located ~24 cm above the corestone and ~24 cm below the protosaprolite.

^b Biotite formulas were calculated assuming that of the total Fe, 3.7% is Fe(III) for the corestone (Murphy et al., 1998), 13% for the middle rindlet, and 30% for the protosaprolite.

^c After Turner et al. (2003).

of Fe enrichment can be detected although dissolution features (e.g., etching) are not seen until the protosaprolite zone. In contrast to the hornblende crystals in the corestone and in the rindlet zone, hornblende crystals in the protosaprolite zone are significantly smaller and dramatically etched (Fig. 6). Similar saw-toothed etching along weathered hornblende cleavage planes has been reported by others (e.g., Berner and Schott, 1982; Anand and Gilkes, 1984; Velbel, 1989). Hornblende grains are extremely difficult to find under SEM above the rindlet–saprolite interface, although XRD patterns indicate that hornblende persists in the first 2 cm of the saprolite, but not beyond. EPMA analyses (2–5 μm spot size) of >300 hornblende grains revealed no compositional changes as a function of distance from the corestone (Fig. 7).

As mentioned before, the rindlet–saprolite interface runs through the middle of the protosaprolite zone (Fig. 2). In the rindlet portion of the protosaprolite zone, primary mineral grains are surrounded by abundant precipitated gibbsite with minor kaolinite identified by elemental ratios measured by EDS and EPMA. Kaolinite becomes more abundant above the saprolite–rindlet boundary. Boxwork replacement of primary iron oxide crystals by iron (oxy)hydroxides (e.g., Nahon, 1986; Velbel, 1989; Delvigne, 1998) was observed only within the protosaprolite zone. Quartz remains relatively pristine throughout the rindlet and the protosaprolite zones (Fig. 4). Specifically, no dissolution channels, no etch pits, and few grain micro-cracks were observed in quartz grains.

Point counting of mineral phases in BSE images using image analysis software was difficult for individual Fe-silicate phases due to overlapping grayscale values, which are a function of the mean atomic number of the sample. Specifically, it was not possible to quantify the Fe-silicate minerals individually due to the partial hydrothermal, pseudomorphic replacement of biotite by chlorite and the similar chemistries (and hence similar average atomic numbers and grayscale values) of the chlorite, biotite, and hornblende in these samples. The volume percentages of these Fe-silicates (as a group) indicates that they are relatively constant over the rindlet zone, but decrease in abundance

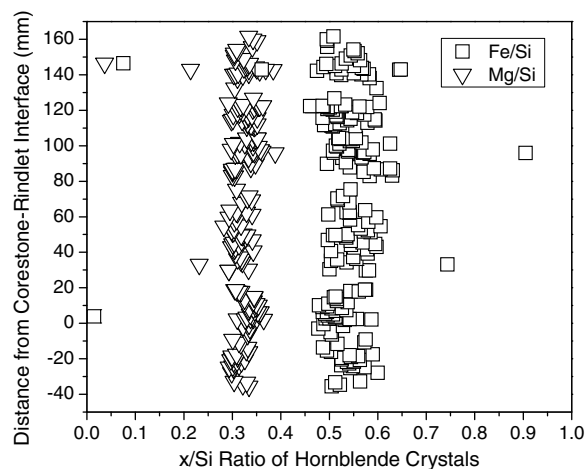


Fig. 7. Fe/Si and Mg/Si ratios of hornblende crystal grains measured by EPMA as a function of distance from the corestone reveal no change in composition across the rindlet zone or across individual rindlets. The negative values on the y axis refer to samples within the corestone.

within the protosaprolite zone (Fig. 8). Apatite, which was readily point-counted (~ 0.6 vol % in the corestone), is entirely lost within the rindlet zone.

Throughout the rindlet zone, the weathering of plagioclase from the calcic cores outward to the sodic rims (Fig. 4b and c) and the oxidation of biotite are readily observed in thin sections under a petrographic microscope. Biotite grains appear more reddish in all of the rindlets than in the corestone, indicating oxidation. In the corestone, no evidence was found to indicate plagioclase weathering (distinct from pre-existing hydrothermal alteration). Conversely, zones of oxidized iron within corestone biotite crystals were documented in X-ray microprobe images (Fig. 9a) of biotite crystals 2.7 cm from the corestone–rindlet interface. Linear least square fitting of the Fe fluorescence counts at each energy measured at each point in the image map was performed to determine the Fe(II) and Fe(III) content of the sample (Fig. 9). Fe(III)–K correlation plots show that areas of higher amounts of Fe(III) have lower K counts (Fig. 10).

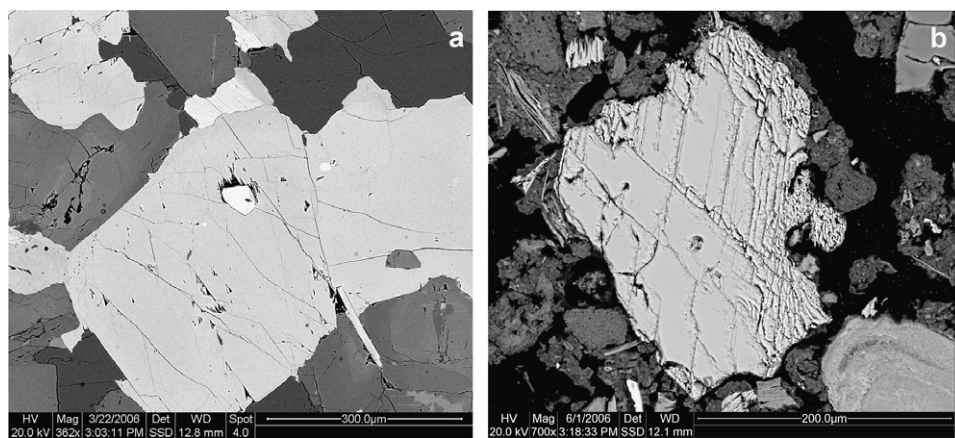


Fig. 6. (a) Backscattered electron images of the corestone reveal pristine hornblende crystals. (b) Hornblende crystals in the protosaprolite zone contain dissolution features along cleavage planes and clumps of gibbsite and some kaolinite surround the crystals.

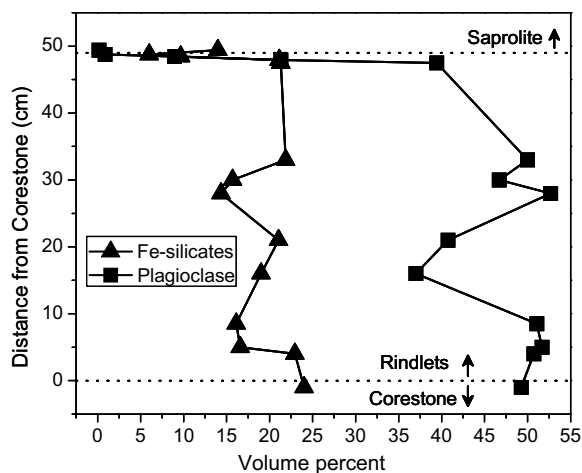


Fig. 8. Volume percent composition of Fe-silicates (hornblende + biotite + chlorite) and of plagioclase with distance from the corestone. Modal analysis was performed by point counting using XT Docu software on backscattered electron images.

Masking of these individual areas show that the center of the biotite grains have approximately constant ratios of Fe(III):K, while the altered regions are localized to the lower K/higher Fe(III) regions (Fig. 11). XANES spectra of these zones were consistent with oxidized biotite and were not consistent with Fe(III)-(hydr)oxide phases nor hornblende (Fig. 12). Oxidized biotite could not be definitively distinguished from chlorite on the basis of XANES spectra alone, but the two phases were easily differentiated by their relative ratios of K to total Fe, which are relatively high in biotite, lower in the oxidized zones, and close to zero in chlorite. Thus, the first weathering reaction observed in this system is the oxidation of biotite within the corestone.

4. DISCUSSION

Based on our microscopic, spectroscopic, chemical, and diffraction data, the following sequence of weathering reactions is proposed. First, within the corestone, diffusion of oxygen into the fresh rock leads to oxidation of Fe(II) to

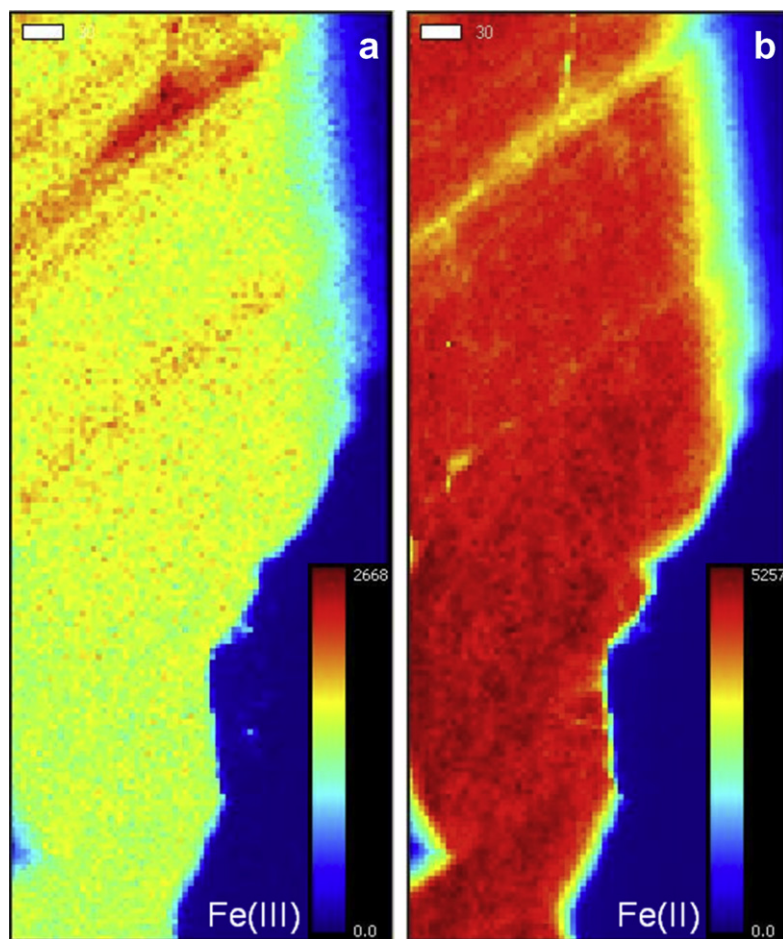


Fig. 9. X-ray microprobe fluorescence maps showing (a) Fe(III) and (b) Fe(II) content in a biotite crystal within the corestone, 2.7 cm from the corestone-rindlet interface. The color scale runs from blue to red indicating least to most Fe(III) or Fe(II). (For interpretation of the references to color in this figure legend, the reader is referred to the web version of this paper.)

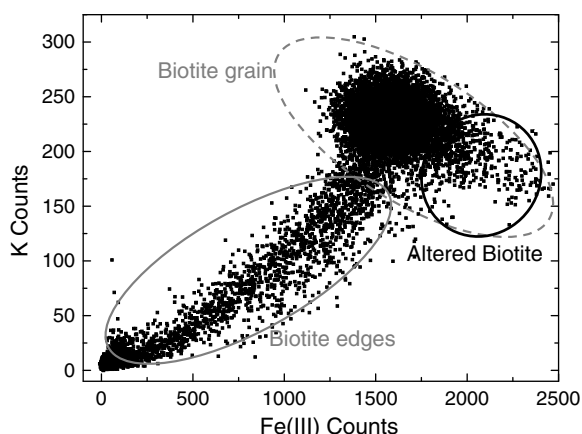


Fig. 10. A plot of K versus Fe(III) fluorescence counts for the biotite grain shown in Fig. 9 shows that areas of higher Fe(III) have lower K. The linear trend of points from the origin to the cluster of points indicating the biotite grain represents a constant ratio in Fe(III):K that is due to thinning along the edges of the biotite crystal. Note that the Fe(III):K ratios in the altered biotite region deviate significantly from the trend in Fe(III):K ratios along the crystal edges and thus cannot be attributed simply to variations in thickness.

Fe(III) within the biotite lattice, which loses K^+ ions from the interlayer to maintain charge balance:

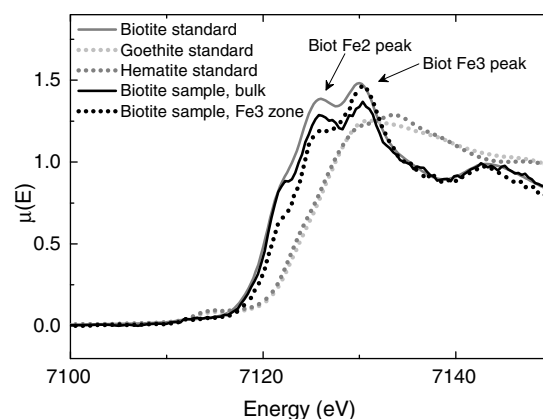
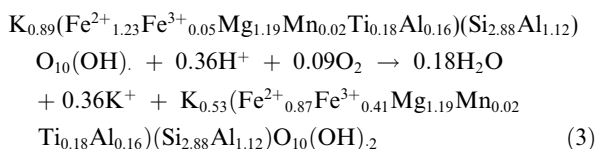


Fig. 12. X-ray absorption near edge spectra (XANES) of fresh and oxidized zones of a single biotite grain within a corestone thin section compared to XANES of mineral standards.

This reaction creates a form of biotite referred to as “altered biotite” by Dong et al. (1998), which is characterized by an expansion of the (001) d -spacing from 10 to 10.5 Å as well as by the oxidation of lattice-bound Fe(II). In the low porosity corestone, this expansion builds up elastic strain energy that leads to fracturing, forming a macro-crack demarcating an individual rindlet. The macro-cracks act as conduits for fluids that penetrate into the rindlets along the macro-crack boundaries to form grain micro-cracks, which tend to congregate along rindlet boundaries and at the corestone–rindlet interface. Rindlet micro-cracks, which fracture multiple mineral grains of multiple phases without

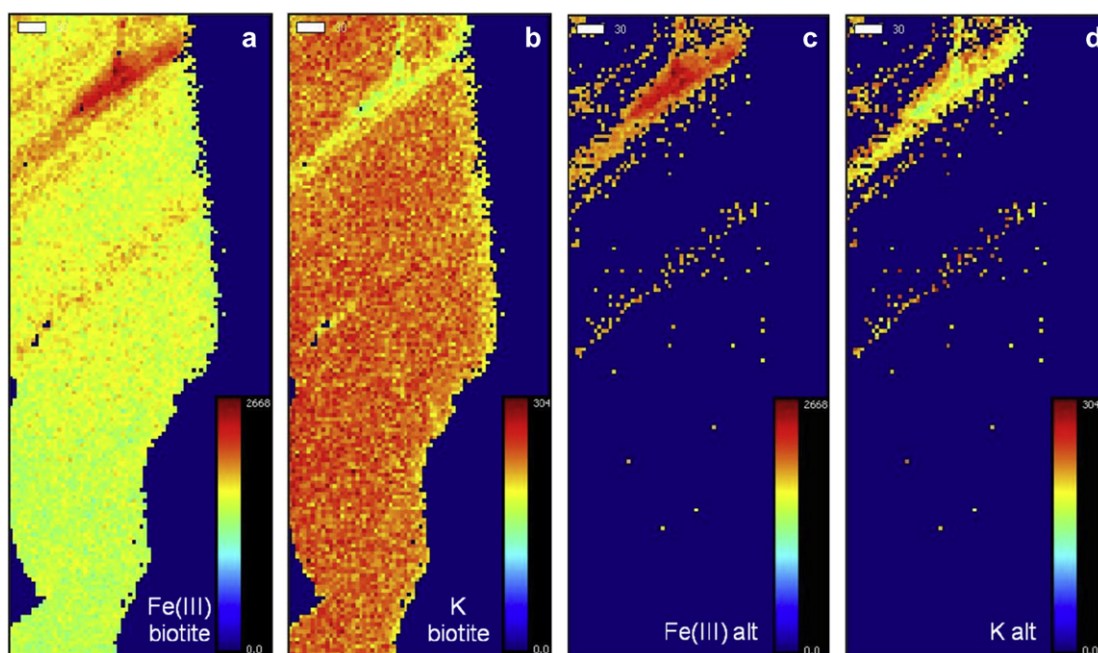
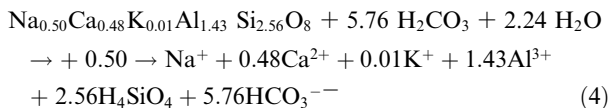
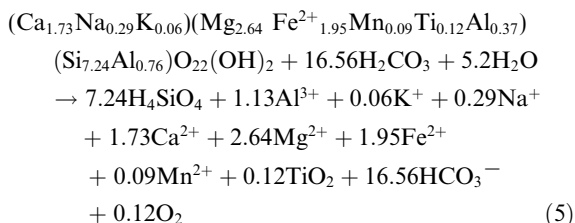


Fig. 11. X-ray microprobe fluorescence maps showing Fe(III) and K content of the biotite grain and altered biotite zones indicated in Fig. 10. (a) Fe(III) and (b) K content in the bulk biotite crystal. (c) Fe(III) and (d) K content of the altered biotite zones. The color scale runs from blue to red indicating least to most Fe(III) or K. (For interpretation of the references to color in this figure legend, the reader is referred to the web version of this paper.)

following grain boundaries, also form after macro-cracking (i.e., they are not observed in the corestone), although the exact cause of these micro-cracks remains unknown. Regardless, rindlet micro-cracks permit penetration of fluids into the rindlet interiors, facilitating further biotite oxidation as well as plagioclase dissolution:



As these reactions progress across the rindlet zone, some saprolitization reactions occur: complete loss of chlorite and oxidation of biotite to its saprolite composition. Within the protosaprolite zone, the final transformation of relatively hard, intact rindlets into soft, disaggregated saprolite takes place. This transformation is accomplished as the remaining plagioclase is lost, all of the hornblende dissolves to completion:



and goethite begins to form. Although hornblende dissolution is insignificant within the rindlet zone, the absence of hornblende in the saprolite indicates that complete dissolution must occur over the ~7 cm protosaprolite zone (Fig. 6b). Although hornblende is also oxidized within the protosaprolite zone, this signal is eclipsed by the complete dissolution of the mineral. Throughout the saprolite, altered biotite weathers to kaolinite (Murphy et al., 1998) and quartz dissolves, developing etch pits (Schulz and White, 1999).

4.1. Weathering gradients and reaction stoichiometry

In a steady state weathering profile, gradients in bulk chemical composition relative to depth are generated by the weathering reactions taking place. Negative gradients (on plots of depth versus chemical composition) indicate a loss of a given element or mineral, while positive slopes indicate an increase. Here we present solid state elemental weathering gradients (b_s in m kg mol^{-1}) following White (2002) from which we extract information about the various weathering reactions occurring over the spheroidally weathering profile.

The mass fraction (e.g., g element g^{-1} rock) of a mobile element that is not incorporated into a secondary mineral after release from a weathering primary mineral, can be modeled as a linear decrease from an initial mass fraction C_0 at depth z_1 to C_w at a shallower depth z_0 (Fig. 13). Here C_0 corresponds to the mass fraction of the element within the protolith (the corestone) and C_w is the mass fraction of the element in a weathered sample at some depth z . The value C_w may differ from the measured value $C_{j,w}$ (Eq. (2)) due to changes in density during weathering. These changes are estimated by normalizing the mass relative to an element that is relatively inert to chemical weathering, here Ti:

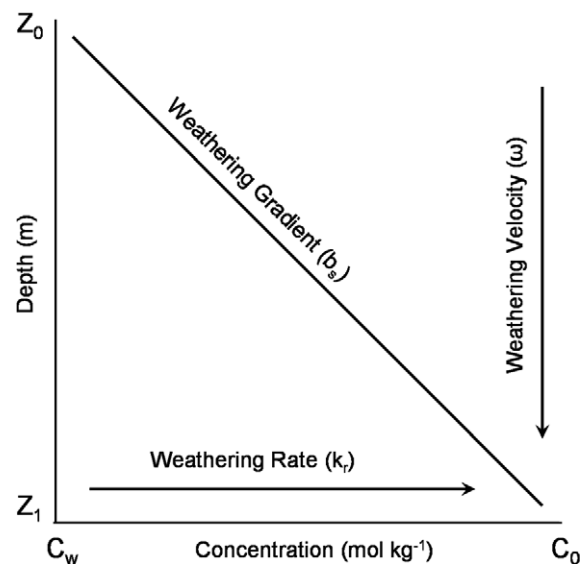


Fig. 13. Schematic diagram (after White, 2002) depicting the distributions of a mobile element in a weathering profile.

$$C_w = C_{j,w} \left(\frac{C_{\text{Ti,p}}}{C_{\text{Ti,w}}} \right) \quad (6)$$

where $C_{\text{Ti,p}}$ (mol kg^{-1}) is the mass fraction of the assumed inert element (Ti) in the protolith and $C_{\text{Ti,w}}$ is the mass fraction of Ti in the weathered material. This normalization is based on the same principles as the calculation of the mass transfer coefficient (Eq. (2)) and can be easily converted:

$$\tau_{\text{Ti},j} = \frac{C_w}{C_{j,p}} - 1 \quad (7)$$

Values of C_w with depth for several elements are shown in Fig. 14 with linear fits. Within the profile studied here, two discrete weathering gradients can be discerned for several elements (Fe, K, Mg, and Mn): the first across the rindlet zone, the second through the protosaprolite zone (Fig. 2). Assuming a steady state profile, differences in gradient for a single element in the protosaprolite versus in the rindlet zone indicate a change in the rate of release of that element, which can signify a change in mineral weathering rates and/or a change in the reactions taking place. For example, the weathering gradient in Fe(II) is significantly shallower across the protosaprolite zone ($b_s = 0.088 \text{ m kg mol}^{-1}$) than in the rindlet zone ($b_s = 2.02 \text{ m kg mol}^{-1}$, Fig. 14a) indicating a more rapid loss of Fe(II) in the protosaprolite and potentially a different reaction. Because the weathering gradients in Fe(III) across the rindlet and protosaprolite zones (Fig. 14b) are reversed with respect to the gradients in Fe(II) (Fig. 14a), it is clear that Fe(II) is lost via oxidation to Fe(III), rather than by removal from the system.

In a multi-mineralic system, multiple weathering reactions may occur simultaneously, each contributing to the elemental weathering gradients in different proportions. The loss of Mg (Fig. 14c) in the rindlet and protosaprolite zones could result from the dissolution of biotite, horn-

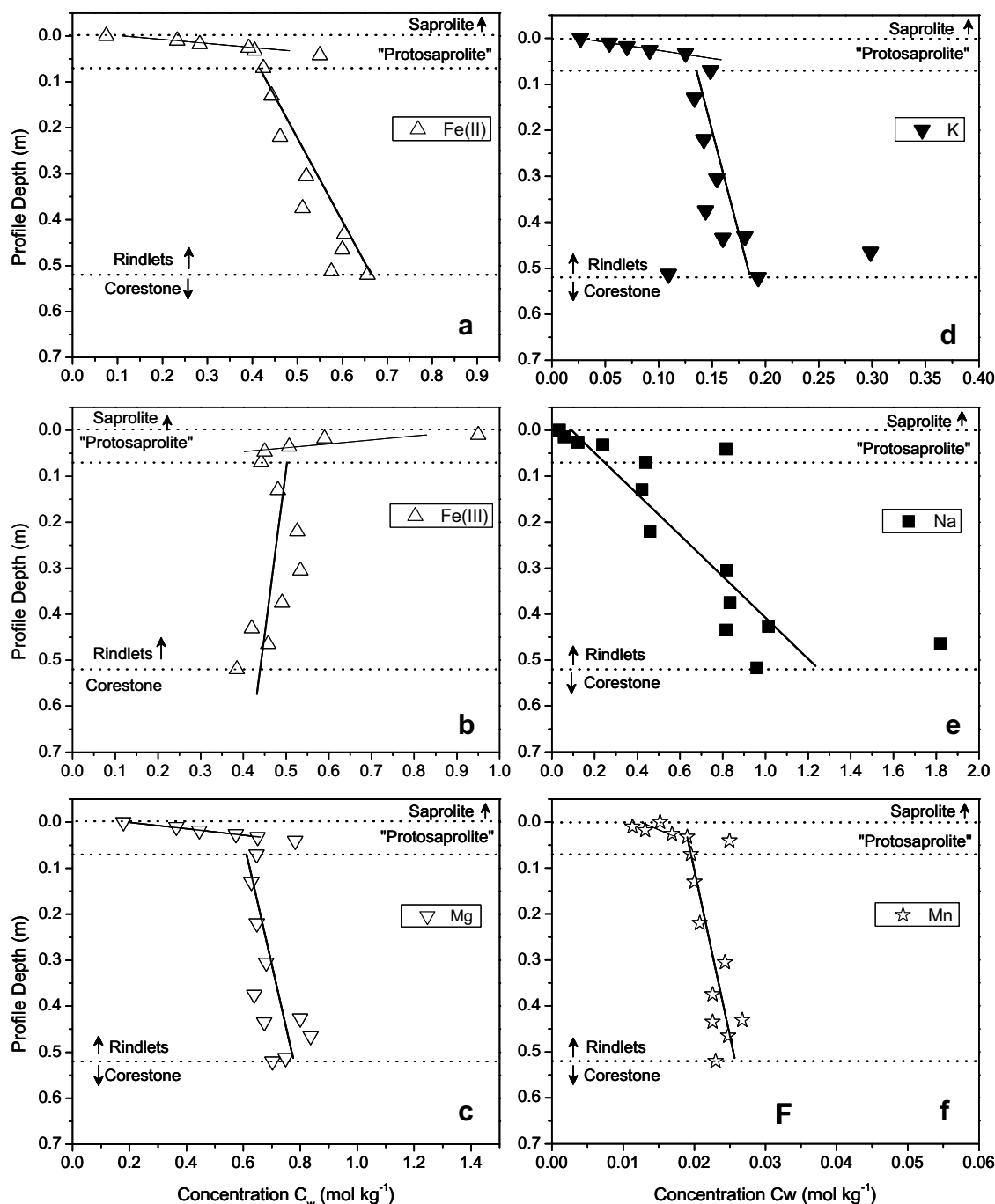


Fig. 14. Weathering gradients (b_s) for (a) Fe(II), (b) Fe(III), (c) Mg, (d) K, (e) Na, and (f) Mn, reveal two distinct trends for most elements: one through the rindlet zone, and one through the protosaprolite zone. Enrichments relative to the parent values seen as positive excursions at the protosaprolite zone were not included in the linear fits. These excursions are thought to be related to the horizontality of the particular rindlet sequence studied combined with the difference in permeability between the saprolite and the rindlet zone. This possibility should be further examined by analyzing sub-vertical rindlet sets from the sides of the corestones. For zones that were subsampled more intensively (protosaprolite, the corestone, and the first 3 rindlets), subsamples from single rindlets were averaged together.

blende, or chlorite, or the oxidation of hornblende. The loss of K (Fig. 14d) could be caused by biotite oxidation or dissolution of biotite or hornblende; and the loss of Mn (Fig. 14f) could indicate dissolution of hornblende or biotite. The loss of Fe(II) over the rindlet zone could be caused by any of the following reactions: dissolution of hornblende, oxi-

dation of Fe(II) in hornblende, dissolution of biotite, oxidation of Fe(II) in biotite, dissolution of chlorite, or oxidation of Fe(II) in chlorite. These reactions involve Fe^{2+} as well as K^+ and/or Mg^{2+} . We can represent these reactions by their stoichiometries with respect to these ions. The stoichiometry of biotite oxidation is 1 mol Fe^{2+} oxidized per mol

K^+ lost and the stoichiometry of hornblende oxidation is 2 mol Fe^{2+} oxidized per mol Mg^{2+} lost.

To estimate the relative importance of the different Fe-silicate weathering reactions occurring within the rindlet zone, we set up and solve a system of equations describing the weathering gradients for several elements (Fe(II), Mg, K, and Mn) as functions of the stoichiometries of the possible reactions:

$$\frac{1}{b_{Fe(II)}} = v_{b,o}^{Fe(II)} M_{b,o} + v_{h,o}^{Fe(II)} M_{h,o} + v_{b,d}^{Fe(II)} M_{b,d} + v_{h,d}^{Fe(II)} M_{h,d} + v_{c,d}^{Fe(II)} M_{c,d} \quad (8)$$

$$\frac{1}{b_K} = v_{b,o}^K M_{b,o} + v_{b,d}^K M_{b,d} + v_{h,d}^K M_{h,d} \quad (9)$$

$$\frac{1}{b_{Mg}} = v_{h,o}^{Mg} M_{h,o} + v_{b,d}^{Mg} M_{b,d} + v_{h,d}^{Mg} M_{h,d} + v_{c,d}^{Mg} M_{c,d} \quad (10)$$

$$\frac{1}{b_{Mn}} = v_{b,d}^{Mn} M_{b,d} + v_{h,d}^{Mn} M_{h,d} \quad (11)$$

Here b_s is a weathering gradient ($m \text{ kg mol}^{-1}$) where $s = \text{Fe(II), K, Mg, or Mn}$ and $v_{i,j}^x$ represent the stoichiometric coefficients for $x = \text{Fe(II), K, Mg, and Mn}$, and subscripts $i = b, h, \text{ or } c$ indicating biotite, hornblende, chlorite, respectively, and $j = o$ or d indicating oxidation or dissolution, respectively. For example, $v_{b,o}^{Fe(II)}$ indicates the moles of Fe(II) “lost” per mol of biotite oxidized. These values are listed in Table 4. M indicates the quantity ($\text{mol m}^{-1} \text{ kg}^{-1}$) of mineral ($b, h, \text{ or } c$) undergoing either oxidation or dissolution (o or d) in the rindlet zone. We

reduce the unknowns from 5 to 4 by assuming that all chlorite is dissolved over the rindlet zone. This is reasonable because chlorite—the least abundant Fe-silicate phase in the bedrock—is not observed in the protosaprolite or saprolite. This assumption gives $M_{c,d} = 0.185 \text{ mol m}^{-1} \text{ kg}^{-1}$ of chlorite dissolved. Solving the system of equations yields $M_{b,d} = -1.0 \text{ mol m}^{-1} \text{ kg}^{-1}$, $M_{h,d} = 0.39 \text{ mol m}^{-1} \text{ kg}^{-1}$, $M_{b,o} = 2.8 \text{ mol m}^{-1} \text{ kg}^{-1}$, $M_{h,o} = -0.01 \text{ mol m}^{-1} \text{ kg}^{-1}$. The negative values for biotite dissolution ($M_{b,d}$) and hornblende oxidation ($M_{h,o}$) likely reflects the sequestration of Mg-within secondary phases or loss of Mg during biotite oxidation, which was not considered here. Vermiculite layers interstratified with altered biotite in the protosaprolite zone are one likely candidate for a Mg sink. This intermediate phase, although detected by XRD and TEM in the saprolite by Murphy et al. (1998) and Dong et al. (1998), were not modeled here because they vary in composition and are a very small component of the total mineralogy. Despite this simplification, these results clearly show that Fe(II) loss across the rindlet zone is dominated by biotite oxidation. Optically, hornblende oxidation does not appear to be significant within the rindlet zone. This conclusion is supported by these calculations and by EPMA results, which do not indicate any loss of cations from hornblende as a function of distance across the rindlet zone (Fig. 7).

The stoichiometric coefficients for Fe and K during biotite oxidation, $v_{b,o}^{Fe(II)}$ and $v_{b,o}^K$, represent an increase in ferric iron in the mineral formula of 26.3%: the observed

Table 4
List of variables for Eqs. (8)–(11)

$v_{b,o}^{Fe(II)}$	0.36	mol mol^{-1}	mol Fe(II) lost during biotite oxidation
$v_{h,o}^{Fe(II)}$	1.95	mol mol^{-1}	mol Fe(II) lost during hornblende oxidation
$v_{b,d}^{Fe(II)}$	1.23	mol mol^{-1}	mol Fe(II) lost during biotite dissolution
$v_{h,d}^{Fe(II)}$	1.95	mol mol^{-1}	mol Fe(II) lost during hornblende dissolution
$v_{c,d}^{Fe(II)}$	0.29 ^a	mol mol^{-1}	mol Fe(II) lost during chlorite dissolution
$v_{b,o}^K$	0.36	mol mol^{-1}	mol K lost during biotite oxidation
$v_{b,d}^K$	0.88	mol mol^{-1}	mol K lost during biotite dissolution
$v_{h,d}^K$	0.06	mol mol^{-1}	mol K lost during hornblende dissolution
$v_{h,o}^{Mg}$	0.973	mol mol^{-1}	mol Mg lost during hornblende oxidation
$v_{b,d}^{Mg}$	1.19	mol mol^{-1}	mol Mg lost during biotite dissolution
$v_{h,d}^{Mg}$	2.637	mol mol^{-1}	mol Mg lost during hornblende dissolution
$v_{c,d}^{Mg}$	3.32 ^a	mol mol^{-1}	mol Mg lost during chlorite dissolution
$v_{b,d}^{Mn}$	0.02	mol mol^{-1}	mol Mn lost during biotite dissolution
$v_{h,d}^{Mn}$	0.09	mol mol^{-1}	mol Mn lost during hornblende dissolution
$M_{b,o}$	2.81	$\text{mol m}^{-1} \text{ kg}^{-1}$	mol biotite oxidized per unit rock
$M_{h,o}$	−0.01	$\text{mol m}^{-1} \text{ kg}^{-1}$	mol hornblende oxidized per unit rock
$M_{b,d}$	−1.05	$\text{mol m}^{-1} \text{ kg}^{-1}$	mol biotite dissolved per unit rock
$M_{h,d}$	0.39	$\text{mol m}^{-1} \text{ kg}^{-1}$	mol hornblende dissolved per unit rock
$M_{c,d}$	0.185	$\text{mol m}^{-1} \text{ kg}^{-1}$	mol chlorite dissolved per unit rock
$b_{Fe(II)}$	2.02	m kg mol^{-1}	Fe(II) weathering gradient
b_K	8.92	m kg mol^{-1}	K weathering gradient
b_{Mg}	2.71	m kg mol^{-1}	Mg weathering gradient
b_{Mn}	72.3	m kg mol^{-1}	Mn weathering gradient

^a Chlorite variables determined from formula of Turner et al. (2003).

difference in oxidation between bedrock biotite and biotite in the deepest saprolite (Murphy et al., 1998). If we assume 3.7% of the biotite iron in the corestone is ferric following Murphy et al. (1998), then convert an additional 26.3% of the ferrous iron to ferric, removing the molar equivalent in K, the resulting composition is consistent the measured biotite compositions (EPMA) in the protosaprolite. These results are consistent with a model in which iron in biotite is oxidizing across the rindlet zone and ejecting K^+ ions to compensate for the loss of electrons. These results also indicate that biotite achieves the oxidation state of the saprolite biotite (Murphy et al., 1998) within the rindlet zone.

When a chemical gradient can be assigned to a mineral weathering reaction, that gradient can be thought of as the weathering front for that particular reaction. Thus, the Na gradient in the rindlet zone defines the plagioclase weathering front and the Fe(II) gradient through the rindlet and protosaprolite zones define the biotite oxidation and hornblende dissolution fronts, respectively. In the saprolite, the K gradient defines the biotite dissolution front (Buss, 2006). Therefore, although the bedrock–saprolite interface (i.e., the rindlet zone) can be thought of as the bedrock weathering front, the system contains individual mineral weathering fronts that occur in different portions of the profile and at different rates (Fig. 15).

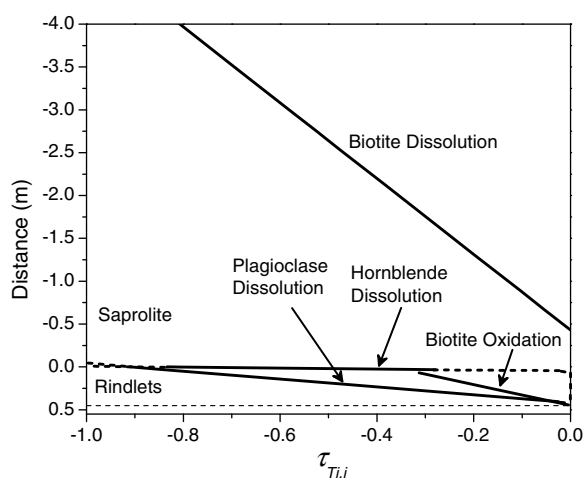


Fig. 15. Semi-schematic diagram indicating the location and gradient of the individual mineral weathering fronts in a generalized profile for the Rio Icacos watershed. $\tau_{Ti,j}$ is the mass transfer coefficient (Eq. (2)) where $j = Na$ (plagioclase dissolution), Fe(II) (biotite oxidation or hornblende dissolution), or K (biotite dissolution). Dotted portions of the lines are extensions of the calculated values. Distance is set to zero at the rindlet–saprolite interface with positive values into the rindlet zone and negative values into the saprolite. The thin dashed line indicates the corestone–rindlet boundary. The biotite dissolution front was calculated from K data from Buss (2006) for a ridgetop saprolite profile near the roadcut studied here. However, this front should be considered approximate because Ti is a structural component of the biotite as well as the normalizing element. The plagioclase, hornblende, and biotite oxidation fronts were calculated from data collected on the roadcut samples in the present study.

4.2. Quantification of mineral weathering rates

Elemental weathering gradients as discussed above can also be used to calculate long-term, average mineral reaction rates. Using the methodology of White (2002) we use the solid state weathering gradients (Figs. 13 and 14) to calculate weathering rates across the rindlet zone for hornblende and plagioclase dissolution and biotite oxidation.

The solid-state reaction rate R for a given mineral in a weathering profile is calculated from the elemental distribution in the profile using the following expression from White (2002):

$$R = 10^{-3} \frac{1}{\phi \beta s} \frac{\omega}{b_s} \quad (12)$$

where ϕ is the mass fraction of the mineral in the weathering material ($g\ g^{-1}$), β is the stoichiometric coefficient of the element in the mineral ($mol\ mol^{-1}$), s is the specific surface area of the mineral ($m^2\ g^{-1}$), b_s is the weathering gradient ($mol\ kg\ mol^{-1}$), and ω is the weathering advance rate ($m\ s^{-1}$). Here the weathering advance rate equals the total denudation rate.

4.3. Biotite weathering

In powder XRD analyses and TEM images, Murphy et al. (1998) and Dong et al. (1998) both noted the presence of an altered biotite phase in the Rio Icacos saprolite having a $d(001)$ spacing of 10.5 Å (compared to the 10.0 Å typical of biotite); higher Al/Si and Fe(III)/Fe(II) ratios; and lower total Fe, Mg, and K than fresh biotite. XRD patterns of these altered biotite grains contain a (060) peak at 1.55 Å indicating a trioctahedral structure. A peak was not observed at 14 Å, characteristic of vermiculite or chlorite (Murphy et al., 1998). Similarly, Mg^{2+} saturation did not yield a 24 Å peak and the 10.5 Å peak did not shift after Mg^{2+} saturation, Mg^{2+} saturation/ethylene glycol solvation, K^+ saturation, or K^+ saturation with heating to 110 °C (Murphy et al., 1998), all traditional indicators of interstratified vermiculite (e.g., Malla and Douglas, 1987; Sawhney, 1989). However, Murphy et al. (1998) identified several 14 Å layers in biotite grains using TEM and interpreted the 10.5 Å $d(001)$ peak and a co-existing 3.37 Å peak as evidence for a randomly interstratified biotite/vermiculite phase (sometimes called hydrobiotite) containing ~12% vermiculite. This interpretation was made based on Méring's principles (summarized by Moore and Reynolds, 1997), which state that randomly interstratified phases will produce reflections between the (001) peaks of the endmembers (e.g., 10.0 Å biotite and 14 Å vermiculite) that are shifted relative to the proportion of the two endmembers in the mixed structure. When Dong et al. (1998) measured altered biotite $d(001)$ spacings with TEM excluding the 14 Å layers, the 10.5 Å spacings were still observed. This result was taken as evidence that the altered biotite is a separate phase, distinct from both fresh biotite and interstratified vermiculite/biotite. Possible causes of the expansion from 10.0 to 10.5 Å were not discussed by Dong et al. (1998).

The altered biotite phase was found in the saprolite but not in the bedrock, and was therefore presumed to form at

the bedrock–saprolite interface (Dong et al., 1998), in other words, within the rindlet zone. Murphy et al. (1998) noted that biotite in the saprolite is oxidized relative to biotite in the bedrock. Gradients in Fe(II) and K across the rindlet zone (Fig. 14a and d) indicate that biotite oxidation occurs there, consistent with the formation of an oxidized “altered biotite” phase. However, we also documented zones of biotite oxidation coupled with K-depletion in the bedrock corestone (Fig. 11), apparently preceding dissolution reactions and porosity development.

The expansion of biotite layers from 10.0 to 10.5 Å during oxidation is consistent with the model proposed by Fletcher et al. (2006). The weathering gradient for Fe(II) through the rindlet zone is consistent with the reaction profile calculated by Fletcher et al. (2006) (Fig. 16). This result, coupled with evidence that biotite oxidation is the first weathering reaction that occurs in the corestone, suggests that biotite oxidation to form altered biotite is most likely the reaction that initiates spheroidal fracturing. Dilation of biotite has been proposed by several researchers as a mechanism for fracturing granite (e.g., Eggler et al., 1969; Isherwood and Street, 1976; Bustin and Mathews, 1979; Dixon and Young, 1981). However, the expansion is typically explained as caused by the formation of vermiculite layers or other clays during biotite weathering (e.g., Eggler

et al., 1969; Isherwood and Street, 1976). The relatively smaller expansion that occurs during the oxidation of biotite may be a novel explanation for reaction-induced fracturing in granitic rock.

A weathering rate for the oxidation of biotite in the rindlet zone can be determined using Eq. (12) and the weathering gradient of Fe(II) across the rindlet zone ($b_s = 2.02 \text{ m kg mol}^{-1}$) and the average weathering advance rate, ω , of 43 m Ma^{-1} (Brown et al., 1995). Other parameters used are $\phi = 0.095 \text{ g g}^{-1}$ (White et al., 1998); specific BET surface area for fresh biotite, $s = 0.1 \text{ m}^2 \text{ g}^{-1}$ (Acker and Bricker, 1992); and $\beta = 0.36 \text{ mol Fe(II) mol}^{-1}$, which is the stoichiometric coefficient of Fe(II) oxidation ($v_{b,o}^{\text{Fe(II)}}$, Table 4). The resulting rate of biotite oxidation within the rindlet sequence is $8.2 \times 10^{-14} \text{ mol m}^{-2} \text{ s}^{-1}$, or $\log R = -13.1$. By comparison, the rate of biotite weathering to kaolinite within the saprolite is $\log R = -15$ (Murphy et al., 1998).

4.4. Plagioclase weathering

Plagioclase weathering occurs steadily across the rindlet and protosaprolite zones, as evidenced by the Na gradient (Fig. 14e), and produces the porosity (void space within remnant plagioclase rims observed in thin sections) that eventually causes the rindlets to disintegrate in the protosaprolite zone. Eq. (12) can again be used to calculate a plagioclase weathering rate from the Na gradient ($b_s = 0.45 \text{ m kg mol}^{-1}$) and mineralogical parameters $\phi = 0.564 \text{ g g}^{-1}$ (White et al., 1998), $\beta = 0.5 \text{ mol Na mol}^{-1}$ (Table 3), and $s = 0.1 \text{ m}^2 \text{ g}^{-1}$. This specific BET surface area is an average value for fresh oligoclase or andesine of 300–600 μm grain size (Holdren and Speyer, 1987), which is within the range of plagioclase grain sizes in the corestone and rindlets (~ 200 – $1000 \mu\text{m}$). The resulting rate of plagioclase weathering is $1.1 \times 10^{-13} \text{ mol m}^{-2} \text{ s}^{-1}$, or $\log R = -13.0$. This rate is faster than that reported by Turner et al. (2003) for rindlet system plagioclase weathering ($\log R = -14.3$ to -14.6). Although Turner et al. (2003) used a range of specific surface areas (0.1 – $1.0 \text{ m}^2 \text{ g}^{-1}$), our rates are still faster even using this range ($\log R = -13.0$ to -14.0). This apparent discrepancy may be a matter of scale. Turner et al. (2003) calculated average plagioclase weathering rates using sections of rindlet sets exhibiting different degrees of weathering from different rindlet sequences within the watershed. One would expect rindlet sets of different orientations, overlying saprolite thicknesses, elevations, and proximity to surface waters to have slightly different weathering rates. Consequently, a rate that incorporates data from several different sample sets can be considered to be an average rate over a larger area. The rate presented here considers a single sub-horizontal rindlet zone atop a corestone and is therefore averaged over a smaller, more densely sampled scale.

4.5. Hornblende weathering

Previous researchers who have studied the Rio Icacos weathering system have noted the absence of hornblende in the saprolite (White et al., 1998; Turner et al., 2003). Hornblende is the most abundant Fe-silicate in the bed-

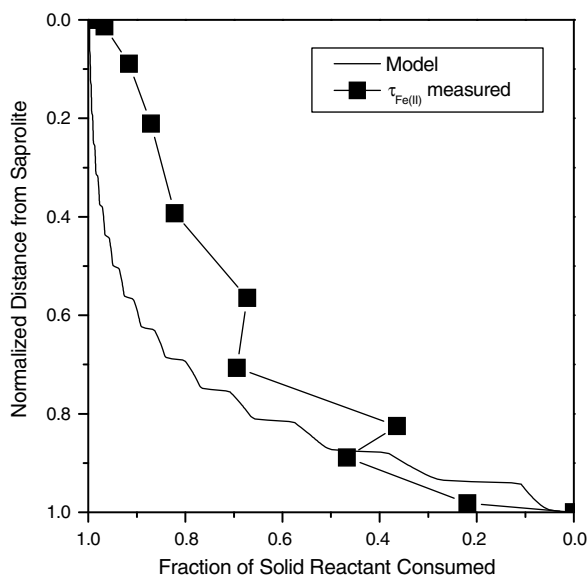


Fig. 16. Fletcher et al. (2006) modeled the oxidation of Fe(II) (as FeO for simplicity) in the corestone hornblende to produce an Fe(III) precipitate, which occurs with an increase in ΔV , causing elastic strain energy to build-up until the corestone fractures to produce a rindlet. The fraction of total Fe(II) that has reacted calculated by Fletcher et al. (2006) is shown here as a continuous line with steps representing the formation of rindlet-defining macro-cracks. Here we compare the profile calculated by the numerical model to the biotite oxidation gradient (the Fe(II) gradient across the rindlet zone, see Fig. 14a), represented as $\tau_{\text{Fe(II)}}$ normalized to the 0–1 scale, where 0 = the saprolite–rindlet interface and 1 = the corestone–rindlet interface. Similar to the numerical model, biotite oxidation begins near the corestone with a large loss of Fe(II), followed by a leveling off near the saprolite.

rock, but the mechanism and location of hornblende weathering has not been previously identified. Pseudomorphic replacement of hornblende by clay minerals such as chlorite, chlorite-saponite, or saponite has been documented in soil and saprolite (Wilson and Farmer, 1970; Anand and Gilkes, 1984), but no widespread evidence for such phase changes was observed in the present samples. Similarly, dissolution of hornblende and re-precipitation of iron (oxy)hydroxides, gibbsite, or kaolinite can occur in soil, saprolite, and weathering rinds (e.g., Velbel, 1989), but was not observed in the rindlet samples: i.e., we observed no etching of the hornblende grains, no boxwork texture or precipitates associated with the rindlet hornblende crystals. In fact, plagioclase and apatite inclusions within hornblende crystals are commonly seen to weather leaving the surrounding hornblende visibly un-weathered (Fig. 4d). EPMA and EDS analyses confirm that the surrounding hornblende is not measurably altered (Fig. 7). These results suggest that hornblende dissolution and subsequent precipitation of Fe(III) (oxy)hydroxides is not the reaction that produces the positive $\Delta V_{\text{reaction}}$ that initiates spheroidal fracturing as suggested by Fletcher et al. (2006).

In some systems, hornblende weathering can also be detected optically by color changes from dark green to pale green due to loss of iron, or to brownish green, due to oxidation of iron (Deer et al., 1962; Wilson and Farmer, 1970). Although hornblende crystals in the outermost rindlets do appear to be slightly oxidized, overall, evidence for hornblende weathering within the rindlet zone is scarce. Therefore, hornblende oxidation is also an unlikely candidate for the reaction that causes the spheroidal fracturing. Although macro- and micro-cracks permit fluid flow into the rindlet zone, total permeability remains low (Turner et al., 2003). Low permeability coupled with high mineral/fluid ratios and increased solute (Al, Si, Na, Ca, Mg) concentrations due to plagioclase and, to a lesser extent, chlorite dissolution are inferred to keep the pore fluid within the rindlet zone saturated with respect to hornblende, preventing dissolution.

To estimate the dissolution rate of hornblende in the protosaprolite using Eq. (12), we consider the gradient in Fe(II) across the protosaprolite zone ($b_s = 0.088 \text{ m kg mol}^{-1}$, Table 4) and mineralogical parameters $\phi = 0.063 \text{ g g}^{-1}$ (White et al., 1998), $\beta = 1.95 \text{ mol Fe(II) mol}^{-1}$ (Table 4), and $s = 0.2 \text{ m}^2 \text{ g}^{-1}$ (Brantley and Mellott, 2000). The resulting rate of hornblende weathering is $6.3 \times 10^{-13} \text{ mol m}^{-2} \text{ s}^{-1}$ ($\log R = -12.2$).

In a steady state profile, the 7 cm thickness of the protosaprolite zone represents a very short time interval relative to the time required to develop the entire profile (about 3 m total thickness at the sampled outcrop). Thus, the complete loss of hornblende over the 7 cm protosaprolite zone implies extremely rapid weathering, which is reflected by the calculated hornblende weathering rate. This rate is faster than other published rates for hornblende weathering in the field, but is within range of laboratory weathering rates (see compilations in White and Brantley, 1995; Brantley, 2004). This similarity to laboratory rates is not so surprising when we consider that the protosaprolite zone has high exposed mineral surface area, high porosity, and high fluid

flux. Typically mineral weathering rates estimated from field data are calculated from watershed fluxes and are averaged over the time period of profile development. In the present study, by densely sampling the weathering profile and calculating the hornblende dissolution rate for only the $\sim 7 \text{ cm}$ thick zone where the reaction occurs, we obtain an *in-situ* rate that is not “diluted” over the entire profile or watershed.

Microorganisms living at depth near the saprolite-bedrock interface may benefit from an increase in availability of inorganic nutrients, Fe(II) in particular, which are released from the bedrock during mineral weathering. The ferrous iron released from hornblende in the protosaprolite zone provides substrate for iron-oxidizing bacteria (Buss et al., 2005). Because most of the Fe(II) within biotite is oxidized *in-situ* rather than released, biotite does not contribute significantly to the flux of Fe(II) available to deep saprolite microorganisms. Iron-oxidizing bacteria fix CO_2 , producing organic carbon to support heterotrophic organisms in the ecosystem. Growth of lithoautotrophs such as iron-oxidizing bacteria in the Rio Icacos saprolite are favored by substrate fluxes and are likely dominant at depth (Buss et al., 2005), contributing to the formation of Fe(III)-(hydr)oxides in the saprolite. The flux of Fe(II) from hornblende dissolution in the protosaprolite could support a maximum growth rate of $4.5 \times 10^{-5} \text{ mol C m}^{-3} \text{ h}^{-1}$ for iron-oxidizing bacteria, based on the model of Buss et al. (2005). Because these bacteria alter the concentrations of Fe(II) and O_2 , they may also affect the rate of spheroidal weathering.

5. CONCLUSIONS

The quartz diorite bedrock in the Rio Icacos watershed weathers spheroidally forming corestones surrounded by zones of concentric, partially weathered rindlets overlain by saprolite. This process produces two distinct weathering interfaces: (1) the bedrock-rindlet interface where the disaggregation is initiated via spheroidal macro-cracking to form rindlets, and (2) the rindlet-saprolite interface where the rindlets disintegrate into saprolite due to extensive micro-cracking and the completion of plagioclase and hornblende weathering. Within the $\sim 7 \text{ cm}$ thick protosaprolite zone, hornblende rapidly dissolves to completion at a rate of $6.3 \times 10^{-13} \text{ mol m}^{-2} \text{ s}^{-1}$, providing the dominant flux of Fe(II) to the saprolite and the saprolite biota. However, within the $\sim 47 \text{ cm}$ rindlet zone, hornblende weathering is insignificant, plagioclase dissolves at a rate of $1.1 \times 10^{-13} \text{ mol m}^{-2} \text{ s}^{-1}$, and biotite is oxidized at a rate of $8.2 \times 10^{-14} \text{ mol m}^{-2} \text{ s}^{-1}$. The oxidation of biotite forms a K-deficient “altered biotite” with an expansion of the $d(001)$ spacing from 10.0 to 10.5 Å. Oxidation of biotite was also identified within individual biotite grains in the bedrock corestone by X-ray microprobe imaging and XANES as the earliest weathering reaction documented in the bedrock. Expansion of biotite during oxidation within the corestone is consistent with the reaction-driven spheroidal fracturing model of Fletcher et al. (2006) and is likely the reaction responsible for initiating the spheroidal fracturing and thus the disaggregation of intact bedrock.

Oxidation of biotite begins when O₂ diffuses into the core-stone, and thus the weathering advance rate is dependent upon the concentration of O₂ in the pore water. This concentration is expected to vary with regolith thickness, providing a positive feedback between denudation and weathering advance rates. The ability to map oxidation states within individual crystals using synchrotron-based techniques has proven invaluable for the observation of incipient weathering reactions within “pristine” bedrock, facilitating identification of rate limiting reactions in coupled processes such as spheroidal weathering.

ACKNOWLEDGMENTS

We thank A.F. White and R.C. Fletcher for helpful discussions and field support; D. Egger and E. Merino for assistance with optical microscopy; M. Angelone and J. Cantolina for analytical assistance; M. Rosario-Torres, J. Troester, and G. Hernandez for field support; and S. Anderson and three anonymous reviewers for comments that helped improve the manuscript. Funding provided by DOE grant no. DE-FG02-05ER15675, the Penn State Biogeochemical Research Initiative for Education (BRIE) supported by NSF-IGERT Grant No. DGE-9972759, and the Penn State Center for Environmental Chemistry and Geochemistry. H.L. Buss acknowledges fellowship support of the NSF Graduate Research Fellowship Program and postdoctoral support from the National Academy of Sciences Research Associateship Program. S.L. Brantley acknowledges support from the Center for Environmental Kinetics Analysis supported by NSF Grant No. CHE-0431328. Portions of this research were carried out at the Stanford Synchrotron Radiation Laboratory, a national user facility operated by Stanford University on behalf of the U.S. Department of Energy, Office of Basic Energy Sciences. The SSRL Structural Molecular Biology Program is supported by the Department of Energy, Office of Biological and Environmental Research, and by the National Institutes of Health, National Center for Research Resources, Biomedical Technology Program.

REFERENCES

- Acker J. G. and Bricker O. P. (1992) The influence of pH on biotite dissolution and alteration kinetics at low temperature. *Geochim. Cosmochim. Acta* **56**, 3073–3092.
- Anand R. R. and Gilkes R. J. (1984) Weathering of hornblende, plagioclase and chlorite in meta-dolerite, Australia. *Geoderma* **34**, 261–280.
- Anderson S. P., Dietrich W. E. and Brimhall G. H. (2002) Weathering profiles, mass-balance analysis, and rates of solute loss: linkages between weathering and erosion in a small, steep catchment. *Geol. Soc. Am. Bull.* **114**, 1143–1158.
- Begle E. A. (1978) *The Weathering of Granite, Llano Region Central Texas*. The University of Texas at Austin.
- Berner R. A. and Schott J. (1982) Mechanism of pyroxene and amphibole weathering: II. Observations of soil grains. *Am. J. Sci.* **282**, 1214–1231.
- Bisdorf E. B. A. (1967) The role of micro-crack systems in the spheroidal weathering of an intrusive granite in Galicia (NW Spain). *Geol. Mijnbouw* **46**, 333–340.
- Boccheciampi R. A., Rivera W. F., Trigo J. E., Brunet J. E., Torres E. O., McKinze W. E. and Rivera L. H. (1977) *Soil Survey of the Humacao Area of Eastern Puerto Rico*. USDA Soil Conservation Service, Washington, DC.
- Brantley S. L. (2004) Reaction kinetics of primary rock-forming minerals under ambient conditions. In *Surface and Groundwater, Weathering, and Soils* (ed. J. I. Drever). Surface and Groundwater, Weathering, and Soils. Elsevier, San Diego, pp. 73–117.
- Brantley S. L. and Mellott N. (2000) Specific surface area and porosity of primary silicate minerals. *Am. Mineral.* **85**, 1767–1783.
- Brimhall G. and Dietrich W. E. (1987) Constitutive mass balance relations between chemical composition, volume, density, porosity, and strain in metasomatic hydrochemical systems: results on weathering and pedogenesis. *Geochim. Cosmochim. Acta* **51**, 567–587.
- Brown E. T., Stallard R., Larsen M. C., Raisbeck G. M. and Yiou F. (1995) Denudation rates determined from the accumulation of in situ-produced ¹⁰Be in the Luquillo Experimental Forest, Puerto Rico. *Earth Planet. Sci. Lett.* **129**, 193–202.
- Buss H. L. (2006) Biogeochemical Weathering of Iron-Silicate Minerals. Ph.D. Thesis, The Pennsylvania State University.
- Buss H. L., Sak P. B., White A. F. and Brantley S. L. (2004) Mineral dissolution at the granite-saprolite interface. In *Elev-enth International Symposium on Water-Rock Interaction* (eds. R. B. Wanty and R. R. I. Seal). Taylor and Francis, Saratoga Springs, NY.
- Buss H. L., Bruns M. A., Schultz M. J., Moore J., Mathur C. F. and Brantley S. L. (2005) The coupling of biological iron cycling and mineral weathering during saprolite formation, Luquillo Mountains, Puerto Rico. *Geobiology* **3**, 247–260.
- Bustin R. M. and Mathews W. H. (1979) Selective weathering of granitic clasts. *Can. J. Earth Sci.* **16**, 215–223.
- Chadwick O. A., Brimhall G. H. and Hendricks D. M. (1990) From black box to a grey box: a mass balance interpretation of pedogenesis. *Geomorphology* **3**, 369–390.
- Chatterjee A. and Raymahashay B. C. (1998) Spheroidal weathering of Deccan Basalt: a three-mineral model. *Q. J. Eng. Geol.* **31**, 175–179.
- Deer W. A., Howie R. A. and Zussman J. (1962) *Rock Forming Minerals Vol. 2: Chain Silicates*. Longmans, London.
- Delvigne J. E. (1998) *Atlas of Micromorphology of Mineral Alteration and Weathering*. Mineralogical Association of Canada, Ottawa.
- Dixon J. C. and Young R. W. (1981) Character and origin of deep arenaceous weathering mantles on the Bega Batholith, south-eastern Australia. *Catena* **8**, 97–109.
- Dixon J. C., Campbell S. W., Thorn C. E. and Darmody R. G. (2006) Incipient weathering rind development on introduced machine-polished granite discs in an Arctic alpine environment, northern Scandinavia. *Earth Surf. Process. Landforms* **31**, 111–121.
- Dong H., Peacor D. R. and Murphy S. F. (1998) TEM study of progressive alteration of igneous biotite to kaolinite throughout a weathered soil profile. *Geochim. Cosmochim. Acta* **62**, 1881–1887.
- Dorn R. (1995) Digital processing of back-scatter electron imagery: a microscopic approach to quantifying chemical weathering. *Geol. Soc. Am. Bull.* **107**, 725–741.
- Dosseto A., Turner S. P. and Chappell J. (in press) The evolution of weathering profiles through time: new insights from uranium-series isotopes. *EPSL*.
- Egger D. H., Larson E. E. and Bradley W. C. (1969) Granites, gneisses, and the Sherman erosion surface, southern Laramie Range, Colorado-Wyoming. *Am. J. Sci.* **267**, 510–522.
- Farmin R. (1937) Hypogene exfoliation in rock masses. *J. Geol.* **45**, 625–635.
- Ferry J. M. (1984) Landforms of spheroidally weathered rock. In *Landscapes of Arizona* (eds. T. L. Smiley, J. D. Nations, T. L. Pewe and J. P. Schafer). University Press of America, Lanham, MD, pp. 415–427.

- Fletcher R. C., Buss H. L. and Brantley S. L. (2006) A spheroidal weathering model coupling porewater chemistry to soil thicknesses during steady-state denudation. *Earth Planet. Sci. Lett.* **244**, 444–457.
- Fritz S. J. and Mohr D. W. (1984) Chemical alteration in the micro weathering environment within a spheroidally-weathered anorthosite boulder. *Geochim. Cosmochim. Acta* **48**, 2527–2535.
- Fritz S. J. and Ragland P. C. (1980) Weathering rinds developed on plutonic igneous rocks in the North Carolina piedmont. *Am. J. Sci.* **280**, 546–559.
- Gilbert G. K. (1904) Domes and dome structure of the High Sierra. *Geol. Soc. Am. Bull.* **15**, 29–36.
- Heald M. T., Hollingsworth T. J. and Smith R. M. (1979) Alteration of sandstone as revealed by spheroidal weathering. *J. Sediment. Petrol.* **49**, 901–909.
- Heimsath A. M., Dietrich W. E., Nishiizumi K. and Finkel R. C. (1999) Cosmogenic nuclides, topography, and the spatial variation of soil depth. *Geomorphology* **27**, 151–172.
- Holdren G. R. and Speyer P. M. (1987) Reaction rate-surface area relationships during the early stages of weathering. II. Data on eight additional feldspars. *Geochim. Cosmochim. Acta* **51**, 2311–2318.
- Isherwood D. and Street A. (1976) Biotite-induced grussification of the Boulder Creek Granodiorite, Boulder County, Colorado. *Geol. Soc. Am. Bull.* **87**, 366–370.
- Larsen E. S. (1948) Batholith and associated rocks of Corona, Elsinore and San Luis Rey quadrangles, southern California. *Geol. Soc. Am. Mem.* **29**, 114–119.
- Le Pera E. and Sorriso-Valvo M. (2000) Weathering and morphogenesis in a mediterranean climate, Calabria, Italy. *Geomorphology* **43**, 251–270.
- Linton D. L. (1955) The problem of tors. *Geograph. J.* **121**, 470–487.
- Malla P. B. and Douglas L. A. (1987) Identification of expanding layer silicates: charge density vs. expansion properties. In *Proc. Int. Clay Conf.* (ed. H. e. a. van Olphen). Clay Minerals Society.
- Mignon P. and Thomas M. F. (2002) Grus weathering mantles—problems of interpretation. *Catena* **49**, 5–24.
- Moore D. M. and Reynolds R. C. (1997) *X-Ray Diffraction and the Identification and Analysis of Clay Minerals*. Oxford University Press, New York.
- Murphy S. F., Brantley S. L., Blum A. E., White A. F. and Dong H. (1998) Chemical weathering in a tropical watershed, Luquillo Mountains, Puerto Rico; II. Rate and mechanism of biotite weathering. *Geochim. Cosmochim. Acta* **62**, 227–243.
- Nahon D. B. (1986) Evolution of iron crusts in tropical landscapes. In *Rates of Chemical Weathering of Rocks and Minerals* (eds. S. M. Coleman and D. P. Dethier). Academic Press, New York, pp. 169–187.
- Ollier C. D. (1967) Spheroidal weathering, exfoliation and constant volume alteration. *Z. Geomorphol.* **11**, 103–108.
- Ollier C. D. (1971) Causes of spheroidal weathering. *Earth Sci. Rev.* **7**, 127–141.
- Ollier C. D. (1988) Deep weathering, groundwater and climate. *Geograf. Ann. Ser. A Phys. Geog.* **70**, 285–290.
- Pavich M. J. (1989) Regolith residence time and the concept of surface age of the Piedmont peneplain. *Geomorphology* **2**, 181–196.
- Riebe C. S., Kirchner J. W. and Finkel R. C. (2003) Long-term rates of chemical weathering and physical erosion from cosmogenic nuclides and geochemical mass balance. *Geochim. Cosmochim. Acta* **67**, 4411–4427.
- Romani J. R. V. and Twidale C. R. (1998) *Formas y paisajes graníticos. Forms and granitic landscapes*. Universidade da Coruna, Coruna, Spain.
- Sawhney B. L. (1989) Interstratification in layer silicates. In *Minerals in Soil Environments* (eds. J. B. Dixon and S. B. Weed), second ed. Soil Sci. Soc. Amer., Madison, WI, pp. 789–828.
- Scarciglia F., Le Pera E. and Critelli S. (2005) Weathering and pedogenesis in the Sila Grande Massif (Calabria, South Italy): from field scale to micromorphology. *Catena* **61**, 1–29.
- Schattner I. (1961) Weathering phenomena in the crystalline of the Sinai in the light of current notions. *Bull. Res. Council Israel G Geo-Sci.* **10G**, 247–266.
- Schulz M. S. and White A. F. (1999) Chemical weathering in a tropical watershed, Luquillo Mountains, Puerto Rico; III. Quartz dissolution rates. *Geochim. Cosmochim. Acta* **63**, 337–350.
- Seiders V. M. (1971) *Geologic Map of the El Yunque Quadrangle, Puerto Rico*. U.S. Geological Survey.
- Sequeira Braga M. A., Paquet H. and Begonha A. (2002) Weathering of granites in a temperate climate (NW Portugal): granitic saprolites and arenization. *Catena* **49**, 41–56.
- Simpson D. R. (1964) Exfoliation of the Upper Pocohontas sandstone, Mercer County, West Virginia. *Am. J. Sci.* **242**, 545–551.
- Thomas M. F. (1974) Granite landforms: a review of some recurrent problems of interpretation. *Problems in Geomorphology: papers in honour of David L. Linton*. Institute of British Geography, London.
- Turner B. F., Stallard R. F. and Brantley S. L. (2003) Investigation of in situ weathering of quartz diorite bedrock in the Rio Icacos basin, Luquillo Experimental Forest, Puerto Rico. *Chem. Geol.* **202**, 313–341.
- USDA NCRS (2002) Soil Survey of Caribbean National Forest and Luquillo Experimental Forest, Commonwealth of Puerto Rico. USDA, Natural Resources Conservation Service, Washington, DC.
- Velbel M. A. (1989) Weathering of hornblende to ferruginous products by a dissolution–reprecipitation mechanism: petrography and stoichiometry. *Clays Clay Miner.* **37**, 515–524.
- von Blanckenburg F., Hewawasam T. and Kubik P. W. (2004) Cosmogenic nuclide evidence for low weathering and denudation in the wet, tropical highlands of Sri Lanka. *J. Geophys. Res.* **109**, F03008.
- Webb S. M. (2006) SMAK: Sam's Microprobe Analysis Kit, V.0.25. Stanford Synchrotron Radiation Laboratory.
- White A. F. (2002) Determining mineral weathering rates based on solid and solute weathering gradients and velocities: application to biotite weathering in saprolites. *Chem. Geol.* **190**, 69–89.
- White A. F. and Brantley S. L. (1995) Chemical weathering rates of silicate minerals: an overview. In *Chemical Weathering Rates of Silicate Minerals* (eds. A. F. White and S. L. Brantley). Mineralogical Society of America, Washington, DC, pp. 1–22.
- White A. F., Blum A. E., Schulz M. S., Vivit D. V., Stonestrom D. A., Larsen M., Murphy S. F. and Eberl D. (1998) Chemical weathering in a tropical watershed, Luquillo Mountains, Puerto Rico: I. Long-term versus short-term weathering fluxes. *Geochim. Cosmochim. Acta* **62**, 209–226.
- Wilson M. J. and Farmer V. C. (1970) A study of weathering in a soil derived from a biotite–hornblende rock, II. The weathering of hornblende. *Clay Minerals* **8**, 435–444.